Title
Influence of Agricultural Managed Aquifer Recharge (AgMAR) and Stratigraphic Heterogeneities on Nitrate Reduction in the Deep Subsurface

Journal
Water Resources Research, 57(5)

ISSN
0043-1397

Authors
Waterhouse, Hannah
Arora, Bhavna
Spycher, Nicolas F
et al.

Publication Date
2021-05-01

DOI
10.1029/2020wr029148

Peer reviewed

Influence of Agricultural Managed Aquifer Recharge (AgMAR) and Stratigraphic Heterogeneities on Nitrate Reduction in the Deep Subsurface

Hannah Waterhouse[1,2,†], Bhavna Arora[3], Nicolas F. Spycher[3], Peter S. Nico[3], Craig Ulrich[3], Helen E. Dahlke[1], and William R. Horwath[1]

[1]Land, Air and Water Resources, University of California at Davis [2]Environmental Science, Policy, and Management, University of California at Berkeley [3]Earth and Enviromental Sciences Area, Lawrence Berkeley National Laboratory

Corresponding author: Hannah Waterhouse (hwaterhouse@berkeley.edu)

†Environmental Science, Policy, and Management, UC Berkeley, Mulford Hall, 130 Hilgard Way, Berkeley, California 94720; Tel: 310-666-3902; ORCID: 0000-0002-8387-4453 Email: *hwaterhouse@berkeley.edu*

Key Points:

- A modeling study shows that AgMAR variably impacts the timing and quantity of nitrate loading to groundwater as a function of stratigraphy
- Under AgMAR, finer textured sediments are important reducing zones acting as permanent sinks of nitrate via denitrification
- Model results pertaining to different denitrification rates under varied ponding conditions are relevant to other landscape settings

This article has been accepted for publication and undergone full peer review but has not been through the copyediting, typesetting, pagination and proofreading process, which may lead to differences between this version and the Version of Record. Please cite this article as doi: 10.1029/2020WR029148.

Abstract

Agricultural managed aquifer recharge (AgMAR) is a strategy whereby surface water is used to intentionally flood croplands to recharge underlying aquifers. However, nitrate (NO_3^-) contamination in agriculturally-intensive regions poses a threat to groundwater resources under AgMAR. We use a reactive transport model to understand the effects of AgMAR management strategies (i.e., by varying the frequency, duration between flooding events, and amount of water) on NO_3^- leaching to groundwater under different stratigraphic configurations and antecedent moisture conditions. We examine the potential of denitrification and nitrogen retention in deep vadose zone sediments (~15 m) using variable AgMAR application rates on two-dimensional representations of differently textured soils, soils with discontinuous bands/channels, and with preferential flow paths characteristic of agricultural fields. Simulations indicate finer textured sediments, alone or embedded within/adjacent to high flow regions, are important reducing zones providing conditions needed for denitrification. Simulation results suggest that applying water all-at-once rather than in increments transports higher concentrations of NO_3^- deeper into the profile, which may exacerbate groundwater quality. This transport into deeper depths can be aggravated by wetter antecedent soil moisture conditions. However, applying water all-at-once also increases denitrification within the vadose zone by promoting anoxic conditions. We conclude that AgMAR can be designed to enhance denitrification in the subsurface and reduce NO_3^- leaching to groundwater, while specifically accounting for lithologic heterogeneity, antecedent soil moisture conditions, and depth to the water table. Our findings are potentially relevant to other systems that experience flooding inundation such as floodplains and dedicated recharge basins.

1 Introduction

Nitrate (NO_3^-) contamination of freshwater resources from agricultural regions is an environmental and human health concern worldwide (Rodell et al. 2018). In agriculturally intensive regions, it is imperative to understand how management practices can enhance or mitigate the effect of nitrogen loading to freshwater systems. In California, managed aquifer recharge on agricultural lands is a proposed management strategy to counterbalance unsustainable groundwater pumping practices. Agricultural managed aquifer recharge (AgMAR) is an approach in which legally and hydrologically available surface water flows are captured and used to intentionally flood croplands with the purpose of recharging underlying aquifers (Kocis and Dahlke, 2017). AgMAR represents a shift away from the normal hydrologic regime wherein high efficiency irrigation application occurs mainly during the growing season. In contrast, AgMAR involves applying large amounts of water over a short period during the winter months. This change in winter application rates has the potential to affect the redox status of the unsaturated (vadose) zone of agricultural regions with implications for nitrogen (N) fate and transport to freshwater resources.

Most modeling studies targeting agricultural N contamination of groundwater are limited to the root zone; these studies assume that once NO_3^- has leached below the root zone, it behaves as a conservative tracer until it reaches the underlying groundwater (Harter et al. 2008, Botros et al. 2012, van der Laan et al. 2013, Baram et al. 2016, Ascott et al. 2016 & 2017) or, these studies employ first order decay coefficients to simplify N cycling reactions (Hanson et al. 2006, Phogat et al. 2014, Salehi et al. 2017). However, recent laboratory and field-based investigations in agricultural systems with deep unsaturated zones have shown the potential for N cycling, in particular denitrification, well below the root zone (Lind and Eiland, 1989, Xiang et al. 2008, Peterson et al. 2013, Haijing et al. 2019) . For example, Haijing et al. (2019) found denitrifying enzyme activity as deep as 12 meters in an agriculturally intensive region in China. Lind and Eiland (1989) reported N_2O production in sediments taken from 20 meter deep cores. Other studies have reported the capability of deep vadose zone sediments to denitrify in anerobic incubations with or without the addition of organic carbon substrates (Peterson et al. 2013). Moreover, in agricultural settings, especially in alluvial basins such as in California with a history of agriculture, large amounts of legacy NO_3^- has built up over years from fertilizer use inefficiencies and exists within the deep subsurface (Pratt et al. 1972, Van Meter et al. 2016, Waterhouse et al. 2020, Nolan et al., 2014, Kent and Landon, 2013, Burow et al., 2013). It is not yet clear how this legacy nitrogen may respond to changing hydrologic regimes and variations in AgMAR practices, and more importantly, if flooding agricultural sites is enhancing nitrate transport to the groundwater or attenuating it by supporting *in situ* denitrification.

Denitrification rates in the subsurface have been reported to vary as a function of carbon and oxygen concentrations, as well as other environmental factors (e.g., pH, temperature, soil texture, iron) (Butterbach-Bahl et al. 2013, Arora et al., 2019, Dwivedi et al., 2018, Yabusaki et al., 2017). While total soil organic carbon typically declines with depth (Syswerda et al. 2011), dissolved organic carbon (DOC) can be readily transported by water lost from the root zone to deeper layers (Bundt et al. 2001, Jardine et al. 2006) and can therefore be available to act as an electron donor for denitrification (Peterson et al. 2013, Cressey et al. 2018). Oxygen concentration in the vadose zone is maintained by advective and diffusive transport, while oxygen consumption occurs via microbial metabolic demand and/or abiotic chemical reactions (Akhavan et al. 2013, Dutta et al. 2015). The effects of drying and wetting cycles on oxygen (O_2) concentrations in the deep subsurface are not well documented. However, in 1 meter column experiments, there is some evidence that O_2 consumption proceeds rapidly as saturation increases and rebounds quickly during dry periods (Dutta et al. 2015). These variations in oxygen concentration can influence N cycling and thus, transport to groundwater. Variability in nitrate concentration has also been linked to heterogeneous subsurface properties, rainfall events, seasonality of flow and other local geochemical conditions across a diversity of settings (e.g., Dwivedi et al., 2017; Rogers et al., 2021; Inamdar et al., 2021; Arora et al., 2013;) However, a gap currently exists in quantifying N attenuation and transport from agriculturally intensive regions with a “deep” vadose zone while accounting for the many competing N cycle reactions and transformations, as impacted by different hydrological regimes imposed under AgMAR.

The application of AgMAR itself can vary in terms of the hydraulic loading and rates used, as well as the duration between flood water applications. These can in turn affect water retention times, O_2 availability, consumption of electron donors (carbon) and consequently, denitrification rates (Akhavan et al. 2013). For example, denitrification rates were found to increase with increased hydraulic loading and with shorter times between flood applications within the vadose zone of a rapid infiltration basin system used for disposing of treated wastewater (Akhavan et al. 2013). In shallow, sandy soils, high flow rates - above an infiltration threshold - were negatively correlated with denitrification rates, suggesting that an optimum infiltration rate exists for a given sediment stratigraphy to maximize NO_3^- reduction (Schmidt et al. 2011). Given the immense stratigraphic heterogeneity in alluvial basins, such as in California’s Central Valley, a range of optimum infiltration rates may exist with implications for managing AgMAR differently based on the geologic setting of the intended site. Therefore, the objectives of this study are to: a) understand the effects of varying stratigraphy and hydrologic regimes on denitrification rates, and b) identify AgMAR management scenarios that increase denitrification rates, such that the potential for N leaching to groundwater is decreased.

Herein, we focus on an agricultural field site in Modesto, California located within the Central Valley of California, which is responsible for California's $46 billion-dollar agricultural economy (CDFA, 2017). The field site typifies the deep vadose zones prevalent in this region, which are characterized by heterogenous layered alluvial sediments intercalated with discontinuous buried clay and carbon rich paleosols (Weissman et al. 2002a, 2002b, Bennett et al. 2006, Chaopricha and Marín-Spiotta, 2014, Marín-Spiotta et al. 2014). These discontinuous, layered features, especially the paleosols and areas of preferential flow, are typically associated with enhanced biogeochemical activity, higher carbon content and availability of metabolic substrates such as nitrogen (Brockman et al. 1992, Bundt et al. 2001). These regions respond to and change depending on environmental conditions such as water content and oxygen concentration *in situ* that are influenced by the hydrologic regime at the surface and may be important for NO_3^- attenuation and reduction prior to reaching the water table. Therefore, this study considers varying hydrologic regimes and stratigraphic variations (including preferential flow paths and discontinuous bands/channels) that are prevalent in the region. More specifically, at the Modesto field site (which is described in more detail below), large amounts of legacy N already reside in the vadose zone, while N fertilizer application and irrigation occurs throughout the spring and summer months. AgMAR, if implemented, occurs during the winter months as water becomes available. Therefore, we focus here on quantifying the effects of AgMAR on N cycling in the deep vadose zone and implications for NO_3^- contamination of groundwater at this characteristic agricultural field site. We also investigate the specific AgMAR application rates that would increase the effectiveness of *in situ* denitrification under different stratigraphic configurations through the development and testing of a reactive transport model. We believe such an analysis provides important insights for the successful application of AgMAR strategies aimed at improving groundwater storage in a changing climate.

2 Materials and Methods

2.1 Modeling Strategy

Reactive transport models can be beneficial tools to elucidating N fate and transport in deep vadose zone environments. Herein, we develop a comprehensive reaction network incorporating the major processes impacting N transport and attenuation, such as aqueous complexation, mineral precipitation and dissolution, and microbially mediated redox reactions. While using the same reaction network, we implement several numerical scenarios to quantify the range of denitrification rates possible under different AgMAR implementation strategies and stratigraphic configurations (Figure 1). For the latter, we used four different stratigraphic configurations with a low permeability layer on top including i) two homogeneous textural profiles, ii) a sand stratigraphy with a discontinuous silt band, iii) a silt stratigraphy with a discontinuous sand band, and iv) a complex stratigraphy more representative of the field conditions investigated by electrical resistance tomography (ERT). The top layer served two purposes, one, it allowed the net infiltration rate to be calibrated to match measured average field infiltration rates of 0.17 cm/hr and two, it represented the expected increase in sediment uniformity expected in ploughed or tilled layers in agricultural settings. While, the impact of the top layer resulted in water being delivered more slowly to the heterogenous sediments below, varying rates of percolation occurred after reaching below the more homogenous layer allowing us to examine the effects of heterogeneity on nitrate transport and fate in the vadose zone. For each stratigraphy, we further varied the frequency and duration of water per application to investigate the impact of different AgMAR implementations that are similar to recent field trials conducted throughout the state (Bachand et al. 2014). In addition, we tested the effect of antecedent moisture conditions on N biogeochemistry within the more complex stratigraphy by setting the model with a wetter initial moisture profile. Overall, a set of 18 simulation experiments were used to isolate and understand the contribution of different AgMAR strategies to enhance or decrease denitrification rates in deep vadose zone environments with homogeneous and banded configurations. A detailed model setup and numerical implementation is provided in Section 2.3. Although our reactive transport analysis was guided by a particular field site that is classified as a "Medium to Good" site for MAR (O'Geen et al., 2015), our aim was not to replicate site conditions in its entirety, but rather to enhance our understanding of how hereogeneity might impact nitrogen transport and fate under MAR.

2.2 Field Site and Datasets

2.2.1 Study Site

The study site is an almond orchard located in California's Central Valley, southwest of Modesto, and north of the Tuolumne River (Figure 2). The surface soil is classified as a Dinuba fine sandy loam (coarse-loamy, mixed, active, thermic, Typic Haploxeralf) (Soil Survey, NRCS). The site is characterized by a Mediterranean climate, with wet winters and hot, dry summers. Average annual temperature and total annual precipitation are 17.5° C and 335 mm, respectively. As suggested above, the vadose zone typifies the valley with contrasting layered sequences of granitic alluvial sedimentary deposits consisting of predominantly silt loams and sandy loams. We therefore use these textures to design our modeled stratigraphic configurations with and without banded layers. The groundwater table in the study area typically occurs around 15 m below ground surface. Soil properties including percent sand, silt, clay, total N, total C, and pH are shown in Table 1.

2.2.2 Characterization of the Deep Vadose Zone

To specifically characterize the textural layers and subsurface heterogeneity at our site, we used electrical resistivity tomography (ERT). ERT profiles were generated along a 150 m transect to 20 m depth prior to flooding to quantify subsurface heterogeneity while the subsurface was relatively dry (Figure 3). Further, to validate the texture profiles generated by the ERT data, a set of six cores were taken along the transect of the ERT line down to nine meters with a Geoprobe push-drill system (Geoprobe Systems, Salina, KS). The first meter of the core was sampled every 25 cm. Thereafter, cores were sampled based on stratigraphy as determined by changes in color or texture. The ERT profiles were used to develop the stratigraphic modeling scenarios and the coring guided the specification of the hydraulic parameters. Redoximorphic features (i.e., changes in concentration and depletion of Fe) were noted throughout the cores.

2.2.3 Soil and Vadose Zone Physical and Chemical Analysis

Texture was analyzed using a modified pipette method whereby 5 g of soil were placed in 50 mL centrifuge tubes with 40 mL of 0.5% sodium phosphate and shaken overnight (Soil Survey Laboratory Methods Manual, 2004). Samples were hand shaken immediately before a 2.5 mL aliquot was taken 11 seconds (sand fraction) and 1 hour and 51 minutes (clay fraction), respectively after shaking and placed in a pre-weighed tin. Tins were oven dried at 105°C overnight and reweighed the next day. Silt fractions were calculated by subtracting the sand and clay fraction from 1.

Nitrate (NO_3^-) and ammonium (NH_4^+) were analyzed by weighing 8-10 g of soil into a 50-mL centrifuge tube and extracted with 2M KCl. Samples were centrifuged and the supernatant was analyzed colorimetrically for soil NO_3^- and NH_4^+ using a UV mini 1240, Shimadzu spectrophotometer as per methods described in Doane and Horwath (2003). Gravimetric water content was determined after soil samples were dried over night at 105° C. Total nitrogen (N) and soil organic carbon (SOC) were measured via combustion on a Costech ECS 4010 CHNSO elemental analyzer using soil samples that were dried at 60° C and pulverized using a ball mill. Samples were checked for carbonates using a 1 mol L^{-1} hydrochloric acid (HCl) solution prior to combustion. A 1:1 water to soil ratio was placed in a falcon tube, shaken for an hour, allowed to settle, and the supernatant pH measured (Thomas, 1996).

Total reactive iron was measured by extracting 1 g of soil with 0.25 M hydroxylamine hydrochloride and 0.25 M HCl, shaking for 1 hour, and reacting with ferrozine (3-(2-pyridyl)-5,6-diphenyl-1,2,4-triazine-4',4"-disulfonate) and measured at 565 nm on a spectrophotometer (Lovley and Phillips 1987, Stookey 1970, Violler et al. 2000). Sulfur and manganese were determined on the supernatant of the same solution by the UC Davis ICPMS. Using a 1:4 ratio of soil to 0.5 M K_2SO_4, dissolved organic carbon (DOC) was extracted, shaken for 1 hour, centrifuged for 10 min at 3000xg, and analyzed on a UV-persulfate total organic carbon analyzer (Phoenix 8000, Tekmar Dohrmann™, Cincinnati, OH).

2.2.4 Acetylene Inhibition Method for Measuring Denitrification Capacity for Model Development

Soil cores taken after the AgMAR event were used to carry out microcosm experiments under anaerobic conditions in a helium atmosphere at 22°C to determine denitrification capacity according to a modified method by Groffman et al. (1999). Briefly, 10 g of air-dried soil from each depth were added to autoclaved 135 ml glass vials. To assess denitrification capacity, 15 ml of sterilized deionized (DI) water was added to the vials without any addition of NO_3^- or carbon substrates. Vials were capped with autoclaved butyl rubber septa, flushed with helium for 10 minutes to create anoxic conditions, after which 10% by volume acetylene was added to the vials to prevent the conversion of N_2O to N_2. Gas samples from the headspace were taken at 30 minutes, 90 minutes, 24 hours, and 3 days. The N_2O and CO_2 measurements after the third and final day of the incubation were used to inform the reaction rate parameters for denitrification. In particular, we used the Q10 equation to adjust the reaction parameters. This is because the Q10 equation can account for the temperature sensitivity of the reaction by calculating the change in the rate of a reaction given a 10 °C change in temperature (Kirschbaum, 1995). Given that our field site temperatures were lower during the winter (mean of 18 °C) than the temperatures at which the denitrification capacity assays were incubated, we estimated the reaction rate using the following equation (Meyer et al. 2018):

$$R_2 = R_1 \, x \, Q_{10}^{(T_2 - T_1)/10} \qquad [1]$$

where R_1 and R_2 are the reaction rates at two different temperatures, T_1 and T_2 (°C), respectively, and Q_{10} is the factor by which the reaction rate increases when the temperature is raised by ten degrees.

2.3 Description of Modeling Framework

2.3.1 Statistical Analysis

Statistical analysis was used to help guide the development of the geochemical reaction network. First, correlation analysis was used to inform the choices of primary geochemical species on the basis of the strength of their relationship with N_2O. Second, on the basis of cluster analysis, stratigraphic configurations with different textural classes were developed. In particular, a Spearman's rank correlation was conducted on the dataset including several physical and geochemical measurements collected on the soil cores. Specific variables included pH, N_2O, NO_3^-, NH_4^+, DOC, Fe, Mn, S, total C, percent sand, silt, and clay, and depth. Variables were standardized using the median and mean absolute distance because most variables were found to be non-normally distributed based on the Kolmogorov-Smirnov test. Correlations between variables with p-values less than 0.05 were considered to be significant. To further understand how the data grouped, a cluster analysis was conducted using the partitioning around medoids method for the same set of variables. Interestingly, data were found to group according to textural classes and depth, which provides a mechanism to develop the modeling strategy around these textural profiles.

2.3.2 Simulation Model

We used the reactive transport code TOUGHREACT V3.32-OMP (Xu et al. 2017, Sonnenthal et al. 2014) to quantify the fate and transport of nitrogen in the deep vadose zone of our study site. For this study, the EOS3 module of TOUGHREACT was used to simulate coupled isothermal, multiphase (water and air) flow and multicomponent reactive transport in the vadose zone (Sonnenthal et al. 2014; Pruess et al. 1999).

2.3.3 Model Setup and Scenarios

Several scenarios were developed based on the soil textures identified in cores and the ERT profiles to provide insights into the effect of stratigraphic heterogeneity and AgMAR management strategies on NO_3^- cycling in the deep subsurface, as described in section 2 above. The five stratigraphies modeled in this study are shown in Figure 1. The limiting layer in the ERT scenario spans 187 to 234 cm-bgs (below ground surface) based on field core observations. For each lithologic profile, three AgMAR management strategies were imposed at the top boundary between 20 m and 150 m of each modeled profile (Figure 1). For each AgMAR management strategy, the same overall amount of water was applied, but the frequency, duration between flooding events, and amount of water applied in each flooding event varied (as shown in Figure 1): a total of 68 cm of water was applied either all at once (scenario S1), in increments of 17 cm once a week for four weeks (scenario S2), in increments of 17 cm twice a week for two weeks (scenario S3), and all three scenarios with an initially wetter moisture profile (Figure 1). Note, that for all scenarios, the same reactions were considered, the water table was maintained at 15 m, and temperature was fixed across depths at 18°C, the mean air temperature for January to February in Modesto.

For all scenarios, the modeling domain consists of a two-dimensional 20-meter deep vertical cross-section extending laterally 2,190 m and including a 190 m wide zone of interest located at its center, thus distant from lateral boundaries on each side by 1,000 m to avoid boundary effects. The zone of interest was discretized using a total of 532 grid blocks with a uniform grid spacing of 1 m along the horizontal axis, and a vertical grid spacing of 0.02 m in the unsaturated zone increasing with depth to 1 m in the saturated zone. A maximum time step of 1 day was specified for all simulated scenarios, although the actual time step was limited by specifying a Courant Number of 0.5, typically resulting in much smaller time steps during early stages of flooding.

Before each flooding simulation, the model was run first to hydrologic steady state conditions including the effect of average (background) rainfall (33 cm year^{-1}). The water table was set at a depth of 15 m by specifying a constant pressure at the bottom model boundary (1.5 x 10^5 Pa at a depth of 20 m), and the model side boundaries (1000 m away from the zone of interest) were set to no-flow conditions.

Under these hydrologic conditions, the model was then run for a 100-yr time period including biogeochemical reactions and fixed atmospheric conditions of O_2 and CO_2 partial pressures at the top boundary, a period after which essentially steady biogeochemical conditions were achieved, including the development of progressively reducing conditions with depth representative of field conditions. For these simulations, the concentrations of dissolved species in background precipitation and in groundwater at the bottom model boundary were fixed, with compositions described in Table 2 to yield similar vertically distributed NO_3^- concentrations as were measured in the soil cores.

Flooding scenarios were then started from the initially steady flow and biogeochemical conditions developed as described above and run for 60 days. For these simulations, a free surface boundary was implemented for scenario S1 where 68 cm of water was applied all at once. In contrast, a specified flux boundary condition was imposed for the scenarios S2-S3, where floodwater applications were broken up over a week. The flood water composition is discussed in Section 2.3.5.

2.3.4 Hydrological and Transport Properties

The Rosetta pedotransfer function model (Schaap et al. 2001) was used to estimate van Genuchten-Mualem parameters for the dominant textural classes identified through cluster analyses (Section 5.1). The hydraulic properties of the top layer were adjusted to match the average infiltration rate of the field experiments of 0.17 cm/hr. Table 3 shows the van Genuchten-Mualem parameters used in this study. Relative permeability values were calculated from the saturated hydraulic conductivity.

2.3.5 Geochemical System

The key geochemical processes included in this study are aqueous speciation, ion exchange, mineral precipitation/dissolution reactions, and microbially mediated redox reactions. The primary species in the modeled reaction network include H^+, H_2O, $SiO_{2\,(aq)}$, Na^+, K^+, Ca^{+2}, Mg^{+2}, HCO_3^-, SO_4^-, Cl^-, $O_{2\,(aq)}$, HS^-, NO_3^-, NO_2^-, $N_{2\,(aq)}$, $NH_{3\,(aq)}$, Al^{+3}, Fe^{+3}, Fe^{+2}, Ba^{+2}, Sr^{+2}, and acetate. The aqueous complexation reactions and their equilibrium constants are listed in Table A1 in the Appendix.

The mineralogy of the agricultural field site (types and amounts of minerals constituting each soil type) was assigned on the basis of previous studies at nearby field locations with similar geology (Harden 1987, Neal et al. 1987, White et al. 1996). Based on these studies, quartz, k-feldspar, albite, montmorillonite, calcite, illite, ferrihydrite, and gibbsite were taken as the main soil constituents. All of these minerals are considered to react under kinetic constraints. The thermodynamic and kinetic constraints for mineral precipitation/dissolution reactions are listed in Tables A2 and A3 in the Appendix. Note that the amount of ferrihydrite in soil was calibrated according to the ferrozine extractions described above, and amounts of other minerals estimated from the previously cited studies (Table A4).

The groundwater composition was taken from analyses reported by Landon and Belitz (2006) for a groundwater well (MOD-01) located near our study site. For simplicity, the background recharge from rainfall was assumed to have the same composition as groundwater except that it was re-equilibrated under atmospheric O_2 and CO_2 conditions prior to infiltration. In addition, the concentrations of N species in the background recharge were set to values determined from our own analyses of N at the top of soil cores. The composition of the flood water was set to that of the background precipitation diluted by a factor of 100 for most constituents except for Cl^{-1}. Ratios of NO_3^- to Cl^{-1} were used to trace the difference between dilution and denitrification effects on NO_3^-.

Denitrification and N_2O production were simulated as aqueous kinetic reactions coupled to the fate of pH, CO_2, Fe, S, NO_3^-, and NH_4^+ based on the Spearman correlation analyses discussed above ($p<0.05$). Apart from pH and nitrate species, Fe and S have been linked to denitrification through chemolithoautotrophic pathways (Arora et al. 2016, Carlson et al. 2012) in addition to heterotrophic denitrification (Butterbach et al. 2013), and are therefore included in our reaction network. Heterotrophic denitrification of NO_3^- to N_2 was represented via a two-step reduction process of NO_3^- to nitrite (NO_2^-) and NO_2^- to dinitrogen (N_2). Additionally, chemolithoautotrophic reduction of NO_3^- to N_2 with Fe (II) and bisulfide (HS^-) as electron donors were implemented. Further, dissolved organic carbon (DOC) was observed throughout the nine-meter profile at our field site, and CO_2 and N_2O profiles showed strong correlation ($p<0.05$). Therefore, DOC degradation was simulated using Monod kinetics, although individual DOC components were not simulated consistent with other modeling studies (Hunter et al. 1998, Arora et al. 2015). In particular, we considered a single solid phase of cellulose in equilibrium with acetate as the source of DOC. Parameters for cellulose dissolution were calibrated using the total organic carbon concentrations obtained for each cluster. Biodegradation of acetate was coupled to multiple terminal electron acceptors, including NO_3^-, Fe (III) and SO_4^{2-} which follow the hierarchical sequence of reduction potential of each constituent implemented by using inhibition terms that impede lower energy-yielding reactions when the higher energy yielding electron acceptors are present. These microbially mediated reactions and their kinetic rate parameters are shown in Table 5.

Rates for denitrification were calibrated using the results from the acetylene inhibition assays as described above. Enzymes involved in denitrification include nitrate reductase, nitrite reductase and nitrous oxide reductase. To remain conservative in our estimates, we chose values typical for oxygen inhibition of nitrous oxide reductase (0.01 mg $O_{2\,(aq)}$ L^{-1}), the most sensitive to oxygen of the enzymes (Bonin et al. 1989).

3 Results

3.1 Statistical Analysis

Spearman rank correlation indicated that pH, DOC, S, NO_3^-, and Fe exhibit significant correlation with N_2O and therefore, these geochemical species were included in the reaction network. Cluster analysis was used to further detect natural groupings in the soil data based on physio-chemical characteristics, textural classes and the total dataset. Cluster analysis revealed three clusters representing distinct depth associated textural classes with varying levels of substrates and biogeochemical activity. Table 5 shows the median and range for N_2O, CO_2, NO_3^-

-N, Fe, S and total organic C for each of the clusters. The first cluster is dominated by sandy loams within the top meter with highest median values of total N_2O, total CO_2, NO_3^- -N, Fe, and total organic C concentrations, indicative of greatest microbial activity and denitrification potential. The second cluster is dominated by silt loams below one meter and had average values of total N_2O, total CO_2, NO_3^- -N, Fe, and total organic C concentrations when compared to the other groups. The third group is dominated by sands and sandy loams below 1 meter and had the lowest median values of total N_2O, total CO_2, NO_3^- -N, Fe, and total organic C concentrations amongst all groups. The clusters were thus automatically grouped by decreasing levels of denitrification and microbial activity. While most concentrations followed a decreasing concentration trend from cluster 1 to 3, the highest median values of S were associated with cluster 2.

3.2 Reactive Transport Model Simulations

3.2.1 Simulated base case conditions and results from scenario S1

Liquid saturation profiles and concentration of key aqueous species predicted at different times for the homogeneous sandy loam column are shown in Figure A1. The sandy loam vadose zone is computed to be 32% saturated with near atmospheric concentrations of O_2. As a result of oxic conditions, model results demonstrate significant residual NO_3^- concentration within the vadose zone (as would be expected). Evolving from these conditions, Figure A1d shows that with flooding scenario S1, water reaches depths of 490 cm-bgs and saturation levels reach 40% in the sandy loam column. Deeper in the column, lower saturation and only small decreases in O_2 concentration are predicted (Figure A1d, e). Calculated concentration profiles show that O_2 introduced with the infiltrating water is persistent at shallow depths down to 100 cm-bgs, below which O_2 declines slightly as floodwater moves below this zone. Model results further indicate higher NO_3^- reduction in the shallow vadose zone including the root zone (down to 100 cm-bgs) with 35% of NO_3^- being denitrified (Figure A1f). Overall, this scenario results in NO_3^- concentration persisting at depth. While other redox reactions, such as iron reduction and HS^- reduction of NO_3^- to N_2, may be important, conditions needed to induce these reactions were not realized in the sandy loam vadose zone due to the high pore gas velocities of the homogenous sandy loam allowing for large amounts of O_2 to penetrate the profile from the incoming oxygenated water.

In comparison to the homogenous sandy loam column, the predicted water content is higher (60% saturated) and O_2 concentration is 53% lower in the vadose zone of the homogenous silt loam column at steady state (Figure A2). This result is expected because of the difference in porosity, with silt loams having higher water holding capacity and lower pore gas velocities compared to sandy loams. Consequently, lower NO_3^- concentration and lower NO_3^-:Cl^- ratio are predicted in the silty loam vadose zone as compared to the sandy loam column (Figures A2 and 6). It is interesting to note that while greater NO_3^- loss and denitrification are predicted for the silty loam vadose zone, carbon concentration associated with the shallow vadose zone (below the root zone) are comparatively lower than for the sandy loam column. Moreover, the calculated pH is lower and iron concentrations are higher in the silt loam profile below the top meter when compared to the same depths within the sandy loam column (Figure 6). This suggests that chemolithoautotrophic reactions could be more important for these finer textured sediments. While both heterotrophic and chemolithoautotrophic reactions would be expected to result in a pH decrease (as expressed in Table 5), the greater decline in pH and concomitant increase in Fe^{+3}

concentration suggests the importance of Fe and S redox cycling associated with the chemolithoautotrophic reactions in silty loam sediments (Figure 6).

Evolving from these steady state conditions, scenario S1 suggests that denitrification is enhanced as floodwater infiltrates into the silt loam column. Model results indicate that saturation increases to 80% from 1 to 4 m depths and O_2 decreases from 2.1 x 10^{-4} mol L^{-1} to 1.7 x 10^{-4} mol L^{-1}, resulting in 43% of the NO_3^- being denitrified for this scenario (Figure 7).

In comparison to the homogeneous profiles, the sandy loam with silt loam channel stratigraphy (SaSi case) has higher calculated water contents (60% saturated) and slightly lower O_2 concentration within and surrounding the silt loam channel than the homogenous sandy loam column under steady state conditions (Figure 4). Calculated NO_3^- concentrations are also similar between the homogenous sandy loam column and SaSi case, except for within and below the silt loam channel where lower NO_3^- concentration was predicted (Figure 4). For scenario S1, water content for the SaSi case increased in a manner similar to the homogenous sandy loam, except for within the silt loam channel, which increased from 60 to 81%. Figure 4 further demonstrates that the infiltrating floodwater resulted in an increase in NO_3^- concentration between 1 and 3 m within the sandy loam textured soil, but a decrease elsewhere. Within the channel itself (1 to 4 m-bgs), lower nitrate and NO_3^-:Cl^- ratio are predicted, suggesting higher rates of denitrification (Figure 4). Overall, the model results indicate that an average of 37% of the NO_3^- concentration is denitrified in the SaSi case 60 days after flooding, with 35% denitrification occurring in the sandy loam matrix and 40% occurring within the silt loam channel. This suggests that the silt loam channel acts as a denitrification hotspot. Furthermore, the silt loam channel has lower carbon and higher Fe^{+3} concentrations similar to the homogenous silt loam column again suggesting the importance of both heterotrophic and chemolithoautotrophic denitrification in these finer textured sediments.

In comparison to the SaSi case, calculated water saturation and O_2 profiles were markedly different between the homogenous silt loam column and the silt loam with sandy loam channel (SiSa case) under steady state conditions (Figure 5). In particular, the sandy loam channel has lower calculated water content (32% saturation) than the homogenous silt loam column (60% saturation). Further, greater gas flux within the channel resulted in 11-19% higher O_2 concentration that penetrated deeper into the vadose zone as compared to the homogeneously textured column. NO_3^- concentration are also estimated to penetrate deeper into the vadose zone in the SiSa case due to the high permeability of the sandy loam channel (Figure 5). While carbon concentration also penetrated deeper in the vadose zone in the SiSa case, higher calculated O_2 concentration did not allow for comparable rates of denitrification below 1 m in this case as observed in the homogenous silt loam profile. This is further confirmed by the lower NO_3^-:Cl^- ratio, which indicates that transport processes dominate biogeochemical fluxes within this column (Figure 5). With scenario S1, the calculated water content increased to 48% saturation while the O_2 concentration remained the same within the channel. The high permeability channel allowed for NO_3^- to move faster and deeper into the vadose zone. Overall, calculated denitrification (41% of NO_3^- was denitrified) was lower in the SiSa case as compared to the homogeneous textured column.

In the simplified ERT stratigraphy, similar patterns were observed such that high permeability channels transported water, O_2, and NO_3^- faster and deeper into the subsurface than low permeability regions (Figure 8). As a result, concentration profiles showed significant variability across the modeled domain even under steady state conditions. For example, the calculated O_2 and NO_3^- concentrations are an order of magnitude lower in the shallow vadose zone below the limiting layer than within the preferential flow channel. Higher NO_3^-:Cl^- ratio within the channel further confirms that preferential flow paths transport higher quantities of dissolved aqueous species without their being impacted by other processes such as denitrification (Figure 8). Other interesting trends are shown by carbon and Fe^{+2} concentrations within the modeled column. Dissolved carbon in particular is predicted to have a lower concentration in the preferential flow channel and the matrix surrounding the channel than below the limiting layer. In contrast, the Fe^{+2} concentration is estimated to be higher in the matrix surrounding the preferential flow channel and below the limiting layer (not shown here). For scenario S1, model results indicate that NO_3^- moved through the preferential flow path faster and deeper into the profile, while the limiting layer acts as a denitrification barrier as evidenced by the decrease in NO_3^-:Cl^- ratio. The highest denitrification was estimated to occur in the matrix adjacent to the preferential flow channel (40% of NO_3^-), followed by intermediate nitrate reduction below the limiting layer and far away from the channel (38%), while the lowest denitrification was estimated to occur within the channel itself (34%). The confluence of higher amounts of C and NO_3^- moving into a reduced zone could be the reason that the matrix surrounding the preferential flow channel has higher denitrification rates, while the regions further away from the preferential flow channel have lower amounts of microbially available C and NO_3^-. In contrast, residence times are too short in the channel to allow for reducing conditions to develop. The ability of the entire vadose zone to denitrify would depend on the overall surface area of preferential flow paths to the rest of the surrounding matrix in the zone of flooding. Overall, we find that low permeability zones alone (e.g., homogeneous silt loam) or embedded within high flow zones (eg., matrix surrounding preferential flow channel, SiSa case) demonstrate highest denitrification rates across all soil profiles.

3.2.2 Results from scenarios S2 and S3

Because the ERT column more closely approximates the heterogenity of our agricultural field site, we use this column to demonstrate the impact of hydraulic loading and application frequency on nitrogen fate and dynamics. Simulated profiles of liquid saturation, NO_3^-, NO_3^-:Cl^- and acetate for the simplified ERT stratigraphy for scenarios S2 (17 cm per week for four weeks) and S3 (17 cm two times per week for two weeks) are shown in Figure 9 and A3. It is interesting to note that AgMAR ponding under scenarios S2 and S3 resulted in fully saturated conditions to persist within the root zone (~down to 100 cm-bgs) only. In comparison, the 68 cm all-at-once application for scenario S1 resulted in fully saturated conditions to occur at even greater depths of 235 cm-bgs (not shown here). This resulted in the NO_3^- front moving deeper into the subsurface to depths of 450 cm-bgs under S1 compared to 150 cm-bgs for scenarios S2 and S3 (Figure 9 & A3). Much lower concentrations of NO_3^- were found at 450 cm-bgs in scenarios S2 and S3 (8×10^{-6} mol NO_3^- L for both S2 and S3) compared to S1 (1×10^{-5} mol NO_3^- L). Thus, larger amounts of water applied all-at-once led to NO_3^- being transported faster and deeper into the profile.

Surprisingly, model results indicate 37% of NO_3^- was denitrified with scenario S1, while 34% and 32% of NO_3^- was denitrified in scenarios S2 and S3, respectively. For scenarios S2 and S3, denitrification was estimated to occur only within the root zone. This was confirmed by NO_3^-:Cl^- ratio that did not show any reduction with depth for these scenarios. A reason for this could be that acetate was not estimated to occur below the root zone, preventing electron donors from reaching greater depths for denitrification to occur. In contrast, model results for S1 indicate that acetate was leached down to 235 cm-bgs below the limiting layer. Overall, model results indicate that NO_3^- did not move as fast or as deep in scenarios S2 or S3; however, the ability of the vadose zone to denitrify was reduced when the hydraulic loading was decreased. The main reason for this was that breaking the application into smaller hydraulic loadings (17 cm) resulted in O_2

concentrations to recover to background atmospheric conditions faster than the larger (68 cm) all-at-once application in scenario S1. In fact, the O_2 concentration differed slightly between S2 and S3. Because O_2 inhibits denitrification, we conclude that these conditions resulted in the different denitrification capacity across application frequency and duration. In summary, we find that larger amounts of water applied all-at-once increased the denitrification capacity of the vadose zone while incremental application of water did not. However, NO_3^- movement to deeper depths was slower under S2 and S3.

3.2.3 Results from varying antecendent moisture conditions

Because initial saturation conditions impact nitrogen leaching, we also simulated the impact of wetter antecedent moisture with 15% higher saturation levels than the base case simulation for the ERT profile. Simulated profiles of liquid saturation, NO_3^-, NO_3^-:Cl^- and acetate for the simplified ERT stratigraphy under wetter conditions are shown in Figure 10. Model results demonstrate that the water front moved faster and deeper into the soil profile under initially wetter conditions for all three scenarios. Within the shallow vadose zone (~150 cm-bgs), across AgMAR scenarios, O_2 concentrations were similar initially, but began differing at early simulated times, with lower O_2 under wetter antecedent moisture conditions than with the base-case simulation. In addition, both oxygen and nitrate concentrations showed significant spatial variation across the modeled column. Notably, nitrate concentrations were 166% higher in the preferential flow channel compared to the sandy loam matrix under wetter conditions, while only 161% difference was observed under the base case simulation (Figure 10).

Nitrate movement followed a pattern similar to water flow, with NO_3^- reaching greater depths with the wetter antecedent moisture conditions. Under S1, however, at 150 cm-bgs, NO_3^- decreased more quickly under the wetter antecedent moisture conditions due to biochemical reduction of NO_3^-, as evidenced by the decrease in NO_3^-:Cl^- ratio, as well as by dilution of the incoming floodwater. In the wetter antecedent moisture conditions, 39%, 31%, and 30% of NO_3^- was denitrified under S1, S2, and S3, respectively. For S1, where water was applied all at once, more denitrification occurred in the wetter antecedent moisture conditions, however, the same was not true of S2 and S3 where water applications were broken up over time. This could be due to the hysteresis effect of subsequent applications of water occurring at higher initial moisture contents, allowing the NO_3^- to move faster and deeper into the profile without the longer residence times needed for denitrification to occur. Thus, wetter antecedent moisture conditions prime the system for increased denitrification capacity when water is applied all at once and sufficient reducing conditions are reached, however, this is counteracted by faster movement of NO_3^- into the vadose zone.

4 Discussion

4.1 Impact of Stratigraphy

Simluations from our study demonstrate that low-permeability zones such as silt loams allow for reducing conditions to develop, thereby leading to higher denitrification in these sediments as compared to high permeability zones such as sandy loams. In fact, the homogenous silt loam profile reported the maximum amount of denitrification occurring across all five stratigraphic configurations (Figure 7). Furthermore, the presence of a silt loam channel in a dominant sandy loam column increased the capacity of the column to denitrify by 2%. Conversely, adding a sandy loam channel into a silt loam matrix decreased the capacity of the column to denitrify by 2%. These relatively simple heterogeneities exemplify how hot spots in the vadose zone can have a small but accumulating effect on denitrification capacity (McClain et al. 2003, Groffman et al. 2009,). Note that differences in denitrification capacity maybe much greater than reported here because of increased complexity and heterogeneity of actual field sites when compared to our simplified modeling domains.

Another observation of interest for silty loams is the prominence of chemolithoautotrophic reactions and Fe cycling observed in these sediments. In comparison, sandy loam sediments showed persistence and transport of NO_3^- to greater depths. A reason for this is that oxygen concentration was much more dynamic in sandy loams, rebounding to oxic conditions more readily than in silt loams, even deep into the vadose zone (5 meters). Dutta et al. (2015) found similar re-aeration patterns in a 1 m column experiment in a sand dominated soil, with re-aeration occurring quickly once drying commenced. Even with the presence of a limiting layer, defined by lower pore gas velocities and higher carbon concentration, a sandy loam channel acted as a conduit of O_2 into the deep vadose zone maintaining a relatively oxic state and thus decreasing the ability of the vadose zone to denitrify. In systems with higher DOC loadings to the subsurface, oxygen consumption may proceed at higher rates creating sub-oxic conditions in the recharge water and more readily create reducing conditions favorable to denitrification in the subsurface (Yeomans et al. 1992, Jahangir et al. 2012, Haijing et al. 2019). We note here that microbial growth, which was not modeled in this study, could also affect the rates of O_2 consumption and re-aeration, which could lead to underestimation of O_2 consumption (Akhavan et al. 2013, Dutta et al. 2015).

Overall, denitrification capacity across different lithologies was shown to depend on the tight coupling between transport, biotic reactions as well as the cycling of Fe and S through chemolithoautotrophic pathways.

4.2 Impact of hydraulic loading and frequency

Under large hydraulic loadings (i.e., S1), overall denitrification was estimated to be the greatest as compared to the lower hydraulic loading scenarios (i.e., S2 or S3). The main reason for the higher denitrification capacity was the significant decline in O_2 concentration estimated for this scenario, whereas such conditions could not be maintained below one meter with lower hydraulic loadings under scenarios S2 and S3. However, nitrate was also transported deeper into the column under S1 as compared to S2 or S3. Tomasek et al. (2019) found the reverse in a floodplain setting, where intermittent indundation with flood water, comparable to our S2 and S3 contexts, resulted in higher rates of denitrification in the zone that was always inundated, due to priming of the microbial community and pulse releases of substrates and electron donors. Future studies examining the impact of AgMAR on denitrification should include processes such as mineralization to see if the same behavior would be observed.

It seems that there may exist a threshold hydraulic loading and frequency of application that could result in anoxic conditions and therefore promote denitrification within the vadose zone for different stratigraphic configurations, although this was not further explored in this study. In another study, Schmidt et al. (2011) found a threshold infiltration rate of 0.7 m d^{-1} for a three-hectare recharge pond located in the Pajaro Valley of central coastal California, such that no denitrification occurred when this threshold was reached. For our simulations, we used a fixed, average infiltration rate of 0.17 cm hr^{-1} for our all-at-once and incremental AgMAR scenarios, however, application rates can be expected to be more varied under natural field settings.

Our results further indicate that the all-at-once higher hydraulic loading, in addition to causing increased levels of saturation and decrease in O_2, resulted in leaching of DOC to greater depths in comparison to lower, incremental hydraulic loading scenarios (i.e., S2, S3). Akhavan et al. 2013 found similar results for an infiltration basin wherein 1.4% higher DOC levels were reported at depths down to 4 m when hydraulic loading was increased. Because organic carbon is typically limited to top 1 m in soils (Dwivedi et al., 2017, 2019), leached DOC that has not been microbially processed could be an important source of electron donors for denitrification at depth. Systems that are already rich in DOC within the subsurface are likely to be more effective in denitrifying, and thus attenuating, NO_3^-, such as floodplains, reactive barriers in MAR settings, or potentially, organically managed agroecosystems (Grau-Martínez et al. 2018).. This finding can also be exploited in agricultural soils by using cover crop and other management practices that increase soluble carbon at depth and therefore remove residual N from the vadose zone (White et al. 2020).

While lower denitrification capacity was estimated for scenarios S2 and S3, an advantage of incremental application was that NO_3^- concentration was not transported to greater depths. Thus, higher NO_3^- concentration was confined to the root zone. If NO_3^- under these scenarios stays closer to the surface, where microbial biomass is higher, and where roots, especially in deep rooted perennial systems such as almonds, can access it, it could ultimately lead to less NO_3^- lost to groundwater. While there is potential for redistribution of this NO_3^- via wetting and drying cycles, future modeling studies should explore multi-year AgMAR management strategies combined with root dynamics to understand N cycling and loading to groundwater under long-term AgMAR.

4.3 Impact of Antecedent Moisture

Simulation results indicate that wetter antecedent moisture conditions promote water and NO_3^- to move deeper into the domain compared to the drier base case simulation. This finding has been noted previously in the literature, however, disagreement exists on the magnitude and extent to which antecedent moisture conditions affect water and solute movement and is highly dependent on vadose zone characteristics. For example, in systems dominated by macropore flow, higher antecedent soil moisture increased the depth to which water and solutes were transported (McCoy et al. 1994, Jarvis et al. 2007). In a soil with textural contrast, where hydraulic conductivity between the topsoil and subsoil decreases sharply, drier antecedent moisture conditions caused water to move faster and deeper into the profile compared to wetter antecedent moisture conditions (Hardie et al. 2011). In our system, where a low-permeability layer lies above a high permeability layer (i.e., sandy loam), the reverse trend was observed. Thus, a tight coupling of stratigraphic heterogeneity and antecedent moisture conditions interact to affect both NO_3^- transport and cycling in the vadose zone, which should be considered while designing AgMAR management strategies to reduce NO_3^- contamination of groundwater. Furthermore, dry and wet cycles affect other aspects of the N cycle that were not included in this study (Xiang et al. 2008). Specifically, the effect of flood water application frequency on mineralization of organic N to inorganic forms should be investigated to assess the full N loading amount to groundwater under AgMAR.

4.4 Application to other similar landscape settings

Although our study was exclusively focused on the impact of AgMAR on groundwater nitrate quality, we believe these findings to be applicable to other similar settings, such as wetlands, floodplains and managed recharge basins. Natural settings such as floodplains and riparian corridors experience ponded water for much of the year and are considered to be denitrification hot spots (Harms and Grimmm 2008; Dwivedi et al., 2018; Vidon et al., 2010). These systems are typically associated with higher DOC and therefore, oxygen consumption is expected to occur at much higher rates than our model setup. This rapid decline in oxygen results in reducing conditions that are favorable to denitrification and efficient nitrate removal. Our model simulations of different hydraulic loadings further demonstrate that changing hydrologic regimes in natural and managed landscapes (e.g., due to dam removal, decrease in river discharge) can substantially alter nitrate consumption versus export from these landscapes.

5 Conclusions

To quantify the influence of AgMAR on groundwater quality, specifically nitrate, we tested different AgMAR application rates under different stratigraphic configurations and antecedent moisture conditions using a reactive transport modeling framework. Simulations of a fixed, moderate infiltration rate indicate that fine textured sediments by themselves (e.g., homogeneous silt loam) or embedded within high permeability zones (e.g., silt loam channel within sandy loam sediments, matrix surrounding preferential flow channels) demonstrate highest denitrification capacity across different stratigraphic configurations. Further, in comparing AgMAR strategies, we found that denitrification capacity increased by applying large amounts of water all-at-once rather than in small incremental amounts. However, applying water all-at-once also pushes NO_3^- deeper into the soil profile compared to applying water in increments, especially if wetter antecedent moisture conditions exist. We conclude that ideal incremental AgMAR applications and hydraulic loadings can be designed to promote denitrification within the root zone and prevent N leaching to groundwater, but this treatment depends on the underlying stratigraphy and site characteristics. Therefore, the site's underlying geology, initial soil moisture content, and depth to the water table influences the water quality outcomes of implementing AgMAR. We recommend future studies to focus on the multiyear effects of AgMAR on N cycling, as well as management practices (i.e. cover cropping) that reduce residual N and increase labile DOC movement into the deep subsurface to increase available electron donors for denitrification.

Acknowledgements

This material is based upon work supported as part of the DOE-SCGSR project, which is funded by the U.S. Department of Energy Biological and Environmental Science Priority Research Area, and as part of the Watershed Function Science Focus Area, which is funded by the U.S. Department of Energy, Office of Science, Office of Biological and Environmental Research, under Award Number DE-AC02-05CH11231 to Lawrence Berkeley National Laboratory. Partial support provided by Lawrence Berkeley Laboratory's Directed Research and Development Program. Additionally, this work was supported by a grant from the Almond Board of California. The TOUGHREACT main input files can be found on the ESS-DIVE repository hosted by Lawrence Berkeley National Lab **at** doi:10.15485/1774081**.** The data gathered for this project would not be possible without the help of technicians, graduate and undergraduate students: Feifan Yang, Zaira Joaquin-Morales, and Rebecca Serata.

Conflict of Interest

The authors declare that they have no conflicts of interest.

References

1. Akhavan, M., Imhoff, P.T., Andres, A.S., Finsterle, S., 2013. Model evaluation of denitrification under rapid infiltration basin systems. J. Contam. Hydrol. 152, 18–34. https://doi.org/10.1016/j.jconhyd.2013.05.007
2. Arora, B., D. Dwivedi, B. Faybishenko, R. Jana, and H. M. Wainwright (2019), Understanding and Predicting Vadose Zone Processes, in *Reviews in Mineralogy and Geochemistry: Reactive transport in Natural and Engineered Systems*, *85* (1), DOI: 10.2138/rmg.2019.85.10.
3. Arora, B., Mohanty, B.P., McGuire, J.T., Cozzarelli, I.M. 2013. Temporal dynamics of biogeochemical processes at the Norman Landfill site. *Water Resources Research*, *49*(10), pp.6909-6926.
4. Arora B., Sengör S.S., Steefel C.I. 2015. A reactive transport benchmark on heavy metal cycling in lake sediments. Comput. Geosci. 19:613–633. doi:10.1007/s10596-014- 9445-8
5. Arora, B., Spycher, N.F., Steefel, C.I., Molins, S., Bill, M., Conrad, M.E., Dong, W., Faybishenko, B., Tokunaga, T.K., Wan, J., Williams, K.H., Yabusaki, S.B., 2016. Influence of hydrological, biogeochemical and temperature transients on subsurface carbon fluxes in a flood plain environment. Biogeochemistry 127, 367–396. https://doi.org/10.1007/s10533-016-0186-8
6. Ascott, M.J., Gooddy, D.C., Wang, L., Stuart, M.E., Lewis, M.A., Ward, R.S., Binley, A.M., 2017. Global patterns of nitrate storage in the vadose zone. Nat. Commun. 8, 1416. https://doi.org/10.1038/s41467-017-01321-w
7. Ascott, M.J., Wang, L., Stuart, M.E., Ward, R.S., Hart, A., 2016. Quantification of nitrate storage in the vadose (unsaturated) zone: a missing component of terrestrial N budgets. Hydrol. Process. 30, 1903–1915. https://doi.org/10.1002/hyp.10748
8. Bachand, P.A.M., Roy, S.B., Choperena, J., Cameron, D., Horwath, W.R., 2014. Implications of using on-farm flood flow capture to recharge groundwater and mitigate flood risks along the Kings River, CA. Environ. Sci. Technol. 48, 13601–13609. https://doi.org/10.1021/es501115c
9. Baram, S., Couvreur, V., Harter, T., Read, M., Brown, P.H., Kandelous, M., Smart, D.R., Hopmans, J.W., 2016. Estimating Nitrate Leaching to Groundwater from Orchards: Comparing Crop Nitrogen Excess, Deep Vadose Zone Data-Driven Estimates, and HYDRUS Modeling. Vadose Zo. J. 15, 0. https://doi.org/10.2136/vzj2016.07.0061
10. Bennett, G.L. Weissman, G.S., Baker, G.S., Hyndman, D.W. 2006. Regional-scale assessment of a sequence-bounding paleosol on fluvial fans using ground-penetrating radar, eastern San Joaquin Valley, California. *GSA Bulletin*: 118 (5-6): 724–732. doi: https://doi.org/10.1130/B25774.1
11. Bonin, P., Gilewicz, M., Bertrand, J.C., 1989. Effects of oxygen on each step of denitrification on Pseudomonas nautica. Can. J. Microbiol. 35, 1061–1064. https://doi.org/10.1139/m89-177
12. Brockman FJ, Kieft TL, Fredrickson JK, Bjornstad BN, Li SW, Spangenburg W, Long PE 1992. Microbiology of vadose zone paleosols in south-central Washington State. Microb Ecol 23:279-301.
13. Botros, Farag E, Onsoy, Yuksel S, Ginn, Timothy R, Harter, T., 2012. Richards Equation - Based Modeling to Estimate Flow and Nitrate Transport in a Deep Alluvial Vadose Zone. Vadoes Zo. J. 11. https://doi.org/10.2136/vzj2011.0145
14. Bundt, M., Widmer, F., Pesaro, M., Zeyer, J., Blaser, P., 2001. Preferential flow paths: Biological “hot spots” in soils. Soil Biol. Biochem. 33, 729–738. https://doi.org/10.1016/S0038-0717(00)00218-2
15. Burow, K.R., Jurgens, B.C., Belitz, K. and Dubrovsky, N.M., 2013. Assessment of regional change in nitrate concentrations in groundwater in the Central Valley, California, USA, 1950s–2000s. Environmental earth sciences, 69(8), pp.2609-2621.
16. Butterbach-Bahl, K., Baggs, E.M., Dannenmann, M., Kiese, R., Zechmeister-Boltenstern, S., 2013. Nitrous oxide emissions from soils: how well do we understand the processes and their controls? Philos. Trans. R. Soc. Lond. B. Biol. Sci. 368, 20130122. https://doi.org/10.1098/rstb.2013.0122
17. CDFA. California Department of Food and Agriculture. Crop Report 2017. http://www.stanag.org/pdf/cropreport/cropreport2017.pdf

18. Carlson, H.K., Clark, lain C., Melnyk, R.A., Coates, J.D., 2012. Toward a mechanistic understanding of anaerobic nitrate-dependent iron oxidation: Balancing electron uptake and detoxification. Front. Microbiol. 3, 1–6. https://doi.org/10.3389/fmicb.2012.00057
19. Chaopricha, N.T., Marín-spiotta, E., 2013. Soil burial contributes to deep soil organic carbon storage. Soil Biol. Biochem. 69, 251–264.
20. Cressey, E.L., Dungait, J.A.J., Jones, D.L., Nicholas, A.P., Quine, T.A., 2018. Soil microbial populations in deep floodplain soils are adapted to infrequent but regular carbon substrate addition. Soil Biol. Biochem. 122, 60–70. https://doi.org/10.1016/j.soilbio.2018.04.001
21. Doane, T.A., Horwath, W.R., 2003. Spectrophotometric Determination of Nitrate with a Single Reagent. Analytical Letters 36, 2713–2722.
22. Doussan et al. 1997 River bank filtration: modelling of the changes in water chemistry with emphasis on nitrogen species. Journal of Contaminant Hydrology 25 (1997) 129-156.
23. Dutta, T., Carles-Brangarí, A., Fernàndez-Garcia, D., Rubol, S., Tirado-Conde, J., Sanchez-Vila, X., 2015. Vadose zone oxygen (O2) dynamics during drying and wetting cycles: An artificial recharge laboratory experiment. J. Hydrol. 527, 151–159. https://doi.org/10.1016/j.jhydrol.2015.04.048
24. Dwivedi, D., Arora, B., Steefel, C.I., Dafflon, B., Versteeg, R. 2018. Hot spots and hot moments of nitrogen in a riparian corridor. *Water Resources Research*, *54*(1), pp.205-222.
25. Dwivedi, D., Steefel, I.C., Arora, B. and Bisht, G., 2017. Impact of intra-meander hyporheic flow on nitrogen cycling. Procedia Earth and Planetary Science, 17, pp.404-407.
26. Dwivedi, D., Tang, J., Bouskill, N., Georgiou, K., Chacon, S.S. and Riley, W.J., 2019. Abiotic and biotic controls on soil organo–mineral interactions: developing model structures to analyze why soil organic matter persists. Reviews in Mineralogy and Geochemistry, 85(1), pp.329-348.
27. Dwivedi, D., Riley, W.J., Torn, M.S., Spycher, N., Maggi, F. and Tang, J.Y., 2017. Mineral properties, microbes, transport, and plant-input profiles control vertical distribution and age of soil carbon stocks. *Soil Biology and Biochemistry*, *107*, pp.244-259.
28. Grau-Martínez, A., Folch, A., Torrentó, C., Valhondo, C., Barba, C., Domènech, C., Soler, A., & Otero, N. (2018). Monitoring induced denitrification during managed aquifer recharge in an infiltration pond. *Journal of Hydrology*, *561*, 123–135. https://doi.org/https://doi.org/10.1016/j.jhydrol.2018.03.044
29. Groffman, P. M., K. Butterbach- Bahl, R. W. Fulweiler, A. J. Gold, J. L. Morse, E. K. Stander, C. Tague, C. Tonitto, and P. Vidon. 2009. Challenges to incorporating spatially and temporally explicit phenomena (hotspots and hot moments) in denitrification models. *Biogeochemistry* **93**:49–77
30. Groffman, P.M., Holland, E.A., Myrold, D.D., Robertson, G.P., Zou, X. 1999. Denitrification. Pages 272-288 in G.P. Robertson, D.C. Coleman, C.S. Bledsoe, P. Sollins (editors). Standard soil methods for long-term ecological research. Oxford University Press, New York, NY, USA.
31. Haijing, Y., Shuping, Q., Wenxu, D., Chunsheng, H., Manevski, K., and Xiaoxin, L. 2019. Denitrification Rate and Controlling Factors for Accumulated Nitrate in the Deep Subsoil of Intensive Farmlands: A Case Study in the North China Plain. Pedosphere. V 29:4. 516-526. https://doi.org/10.1016/S1002-0160(17)60472-7.
32. Handley KM, VerBerkmoes NC, Steefel CI et al (2013) Bios- timulation induces syntrophic interactions that impact C, S and N cycling in a sediment microbial community. ISME J 7:800–816. doi:10.1038/ismej.2012.148
33. Hanson, B.R., Šimůnek, J., Hopmans, J.W., 2006. Evaluation of urea-ammonium-nitrate fertigation with drip irrigation using numerical modeling. Agric. Water Manag. 86 (1), 102–113.
34. Harden G.W., 1987. Soils Developed in Granitic Alluvium near Merced, California. U.S. GEOLOGICAL SURVEY BULLETIN 1590-A
35. Hardie, M. A., Cotching, W. E., Doyle, R. B., Holz, G., Lisson, S., & Mattern, K. (2011). Effect of antecedent soil moisture on preferential flow in a texture-contrast soil. *Journal of Hydrology*, *398*(3–4), 191–201. https://doi.org/10.1016/j.jhydrol.2010.12.008
36. Harter, T., Onsoy, Y.S., Heeren, K., Denton, M., Weissmann, G., Hopmans, J.W., Horwath, W.R., 2008. Deep vadose zone hydrology demonstrates fate of nitrate in eastern San Joaquin Valley. Calif. Agric. 59, 124–132. https://doi.org/10.3733/ca.v059n02p124
37. Harms, T.K. and Grimm, N.B., 2008. Hot spots and hot moments of carbon and nitrogen dynamics in a semiarid riparian zone. Journal of Geophysical Research: Biogeosciences, 113(G1).
38. Helgeson HC, Delany JM, Nesbitt HW, Bird DK (1978) Sum- mary and critique of the thermodynamic properties of rock- forming minerals. Am J Sci 278:229

39. Hunter K.S., Wang Y., Van Cappellen P. 1998. Kinetic modeling of microbially-driven redox chemistry of subsurface environments: coupling transport, microbial metabolism and geochemistry. J. Hydrol. 209:53–80. doi:10.1016/ S0022-1694(98)00157-7
40. Inamdar, S., Peipoch, M., Gold, A.J., Lewis, E., Hripto, J., Sherman, M., Addy, K., Merritts, D., Kan, J., Groffman, P.M. and Walter, R., 2021. Ghosts of landuse past: legacy effects of milldams for riparian nitrogen (N) processing and water quality functions. Environmental Research Letters, 16(3), p.035016.
41. Jardine, P.M., Mayes, M. a., Mulholland, P.J., Hanson, P.J., Tarver, J.R., Luxmoore, R.J., McCarthy, J.F., Wilson, G. V., 2006. Vadose Zone Flow and Transport of Dissolved Organic Carbon at Multiple Scales in Humid Regimes. Vadose Zo. J. 5, 140. https://doi.org/10.2136/vzj2005.0036
42. Jahangir, M.M.R., Khalil, M.I., Johnston, P., Cardenas, L.M., Hatch, D.J., Butler, M., Barrett, M., O'flaherty, V., Richards, K.G., 2012. Denitrification potential in subsoils: A mechanism to reduce nitrate leaching to groundwater. Agric. Ecosyst. Environ. 147, 13–23. https://doi.org/10.1016/j.agee.2011.04.015
43. Jarvis, N. J. (2007). A review of non-equilibrium water flow and solute transport in soil macropores: Principles, controlling factors and consequences for water quality. *European Journal of Soil Science*, *58*(3), 523–546. https://doi.org/10.1111/j.1365-2389.2007.00915.x
44. Kent, R. and Landon, M.K., 2013. Trends in concentrations of nitrate and total dissolved solids in public supply wells of the Bunker Hill, Lytle, Rialto, and Colton groundwater subbasins, San Bernardino County, California: Influence of legacy land use. Science of the total environment, 452, pp.125-136.
45. Kirschbaum, M.U.F., 1995. The temperature dependence of soil organic matter decomposition, and the effect of global warming on soil organic C storage. Soil Biol. Biochem. 27, 753–760. https://doi.org/10.1016/0038-0717(94)00242-S
46. Kocis, T.N., Dahlke, H.E., 2017. Availability of high-magnitude streamflow for groundwater banking in the Central Valley, California. Environ. Res. Lett. 12. https://doi.org/10.1088/1748-9326/aa7b1b
47. Landon M.K., Belitz K. 2006, Ground-Water Quality Data in the Central Eastside San Joaquin Basin 2006: Results from the California GAMA Program. USGS Data Series 325, In cooperation with the California State Water Resources Control Board
48. Lind, A.M., Eiland, F. Microbiological characterization and nitrate reduction in subsurface soils. *Biol Fert Soils* **8,** 197–203 (1989). https://doi.org/10.1007/BF00266479
49. Lovley, D.R., Phillips, E.J.P., 1987. Rapid assay for microbially reducible ferric iron in aquatic sediments. Appl. Environ. Microbiol. 53, 1536–1540. https://doi.org/10.1007/BF01611203
50. Maggi et al. 2008 A mechanistic treatment of the dominant soil nitrogen cycling processes: Model development, testing, and application. JOURNAL OF GEOPHYSICAL RESEARCH, VOL. 113, G02016, doi:10.1029/2007JG000578, 2008
51. Marín-Spiotta, E., Chaopricha, N.T., Plante, A.F., Diefendorf, A.F., Mueller, C.W., Grandy, A.S., Mason, J.A., 2014. Long-term stabilization of deep soil carbon by fire and burial during early Holocene climate change. Nat. Geosci. 7, 428–432. http://dx.doi.org/10. 1038/ngeo2169.
52. Mayer KU, Frind EO, Blowes DW (2002) Multicomponent reactive transport modeling in variably saturated porous media using a generalized formulation for kinetically controlled reactions. Water Resour Res 38:13–1–13–21. doi: 10.1029/2001WR000862
53. McClain, M. E., et al. 2003. Biogeochemical hot spots and hot moments at the interface of terrestrial and aquatic ecosystems. *Ecosystems* **6**:301–312.
54. McCoy, E.L., Boast, C.W., Stehouwer, R.C., Kladivko, E.J., 1994. Macropore hydraulics: taking a sledgehammer to classical theory. In: Lal, R., Stewart, B.A. (Eds.), Soil Processes and Water Quality. Lewis Publishers, Boca Raton. p. 303-348.
55. Meyer, N., Meyer, H., Welp, G., Amelung, W., 2018. Soil respiration and its temperature sensitivity (Q10): Rapid acquisition using mid-infrared spectroscopy. Geoderma 323, 31–40. https://doi.org/10.1016/j.geoderma.2018.02.031
56. Morel FMM, Hering JG (1993) Principles and applications of aquatic chemistry. Wiley, New York
57. Neal, R.H., G . Sposito, K.M. Holtzclaw, and S.J. Traina. 1987. Selenite adsorption on alluvial soils: I. Soil composition and pH effects. Soil Sci. Soc. Am. J. 51:1161-1165
58. Nolan, B.T., Gronberg, J.M., Faunt, C.C., Eberts, S.M. and Belitz, K., 2014. Modeling nitrate at domestic and public-supply well depths in the Central Valley, California. Environmental science & technology, 48(10), pp.5643-5651.
59. O'Geen, a. T., Saal, M., Dahlke, H., Doll, D., Elkins, R., Fulton, A., Fogg, G., Harter, T., Hopmans, J. W., Ingels, C., Niederholzer, F., Solis, S. S., Verdegaal, P., & Walkinshaw, M. (2015). Soil suitability index

identifies potential areas for groundwater banking on agricultural lands. *California Agriculture*, *69*(2), 75–84. https://doi.org/10.3733/ca.v069n02p75

60. Palandri JL, Kharaka YK (2004) A compilation of rate param- eters of water-mineral interaction kinetics for application to geochemical modeling. U.S. geological survey open file report 2004–1068, Menlo Park
61. Palmer K, Drake HL, Horn MA (2010) Association of novel and highly diverse acid-tolerant denitrifiers with N2O fluxes of an acidic fen. Appl Environ Microbiol 76:1125–1134. doi:10.1128/AEM.02256-09
62. Parkhurst DL, Appelo CAJ (1999) User's guide to PHREEQC (version 2)—a computer program for speciation, batch- reaction, one-dimensional transport, and inverse geo- chemical calculations. Denver, CO
63. Peterson, M. E., Curtin, D., Thomas, S., Clough, T. J., & Meenken, E. D. (2013). Denitrification in vadose zone material amended with dissolved organic matter from topsoil and subsoil. *Soil Biology and Biochemistry*, *61*(3), 96–104. https://doi.org/10.1016/j.soilbio.2013.02.010
64. Phogat, V., Skewes, M.A., Cox, J.W., Sanderson, G., Alam, J., Simunek, J. "Seasonal simulation of water, salinity and nitrate dynamics under drip irrigated mandarin (Citrus reticulata) and assessing management options for drainage and nitrate leaching." *Journal of Hydrology* 513 (2014): 504-516.
65. Pratt, P.F., Jones, W., Hunsaker, V.E., 1972. Nitrate in Deep Soil Profiles in Relation to Fertilizer Rates and Leaching Volume. J. Environ. Qual. 1, 97–102.
66. Pruess, K., Oldenburg, C., Moridis, G., 1999. TOUGH2 User's Guide, Version 2.0. Lawrence Berkeley National Laboratory Report LBNL-43134.
67. Reed MH, Palandri JL (2006) SOLTHERM.H06, a database of equilibrium constants for minerals and aqueous species. University of Oregon, Eugene
68. Rickard D (2006) The solubility of FeS. Geochim Cosmochim Acta 70:5779–5789. doi:10.1016/j.gca.2006.02.029
69. Rodell, M., Famiglietti, J.S., Wiese, D.N., Reager, J.T., Beaudoing, H.K., Landerer, F.W., Lo, M.-H., 2018. Emerging trends in global freshwater availability. Nature 1. https://doi.org/10.1038/s41586-018-0123-1
70. Rogers, D.B., Newcomer, M.E., Raberg, J.H., Dwivedi, D., Steefel, C., Bouskill, N., Nico, P., Faybishenko, B., Fox, P., Conrad, M. and Bill, M., 2021. Modeling the impact of riparian hollows on river corridor nitrogen exports.
71. Salehi, A., Navabian, M., Varaki, M.E., Pirmoradian, N., 2017. Evaluation of HYDRUS-2D model to simulate the loss of nitrate in subsurface controlled drainage in a physical model scale of paddy fields. Paddy Water Environ. 15, 433–442. https://doi.org/10.1007/s10333-016-0561-z
72. Schaap, M.G., Leij, F.J., van Genuchten, M.T. 2001. Rosetta: a computer program for estimating soil hydraulic parameters with hierarchical pedotransfer functions. J. Hydrol. 251, 163-176
73. Schmidt, C.M., Fisher, A.T., Racz, A.J., Lockwood, B.S., Huertos, M.L., 2011. Linking denitrification and infiltration rates during managed groundwater recharge. Environ. Sci. Technol. 45, 9634–9640. https://doi.org/10.1021/es2023626
74. Shock EL, Koretsky CM (1993) Metal-organic complexes in geochemical processes: calculation of standard partial molal thermodynamic properties of aqueous acetate complexes at high pressures and temperatures. GeochimCosmochimActa 57:4899–4922. doi:10.1016/0016-7037(93)90128-J
75. Shock EL, Sassani DC, Willis M, Sverjensky DA (1997) Inor- ganic species in geologic fluids: correlations among stan- dard molal thermodynamic properties of aqueous ions and hydroxide complexes. Geochim Cosmochim Acta 61:907–950. doi:10.1016/S0016-7037(96)00339-0
76. SNL (2007) Qualification of thermodynamic data for geo- chemical modeling of mineral-water interactions in dilute systems. Las Vegas, Nevada
77. Soil Survey Laboratory Methods Manual. 2004. Texture by Pipette Analysis. Soil Survey Investigations Report No. 42. V. 4. p. 14-21.
78. Soil Survey Staff, Natural Resources Conservation Service, United States Department of Agriculture. Web Soil Survey. Available online at the following link: http://websoilsurvey.sc.egov.usda.gov/. Accessed [07/21/2019].
79. Sonnenthal, Eric, Spycher, Nicolas, and USDOE. *TOUGHREACT (TREACT) v3.32*. Computer software. USDOE. 28 Feb. 2014. Web. doi:10.11578/dc.20190130.1.
80. Stookey, L.L., 1970. Ferrozine-A New Spectrophotometric Reagent for Iron. Anal. Chem. 42, 779–781. https://doi.org/10.1021/ac60289a016
81. Syswerda, S.P., Corbin, A.T., Mokma, D.L., Kravchenko, A.N., Robertson, G.P. 2011. Agricultural management and soil carbon storage in surface versus deep layers. Soil Sci. Soc. Amer. Journal. 75: 92-101.

82. Thomas, G., 1996. Soil pH and soil acidity. In: Sparks, D.L. (Ed.), Methods of soil analysis. Part 3. Chemical methods. Soil Sci. Soc. Am.pp. 475–490 (Madison WI).
83. Tomasek, A. A., Hondzo, M., Kozarek, J. L., Staley, C., Wang, P., Lurndahl, N., & Sadowsky, M. J. (2019). Intermittent flooding of organic-rich soil promotes the formation of denitrification hot moments and hot spots. *Ecosphere*, *10*(1). https://doi.org/10.1002/ecs2.2549
84. van der Laan, M., Annandale, J.G., Bristow, K.L., Stirzaker, R.J., Du Preez, C.C., Thorburn, P.J., 2013. Modelling nitrogen leaching: Are we getting the right answer for the right reason? Agric. Water Manag. 133, 74–80. https://doi.org/10.1016/j.agwat.2013.10.017
85. Vidon, P., Allan, C., Burns, D., Duval, T.P., Gurwick, N., Inamdar, S., Lowrance, R., Okay, J., Scott, D. and Sebestyen, S., 2010. Hot spots and hot moments in riparian zones: potential for improved water quality management 1. JAWRA Journal of the American Water Resources Association, 46(2), pp.278-298.
86. Viollier, E., Inglett, P. W., Hunter, K., Roychoudhury, A. N., & Cappellen, P. Van. (2000). *The Ferrozine method revisted*. *15*, 785–790. https://doi.org/10.1016/S0883-2927(99)00097-9
87. Van Meter, K.J., Basu, N.B., Veenstra, J.J. and Burras, C.L., 2016. The nitrogen legacy: emerging evidence of nitrogen accumulation in anthropogenic landscapes. Environmental Research Letters, 11(3), p.035014.
88. Waterhouse H, Bachand S, Mountjoy D, Choperena J, Bachand P, Dahlke H, Horwath W. 2020. Agricultural managed aquifer recharge — water quality factors to consider. Calif Agr 74(3):144-154. https://doi.org/10.3733/ca.2020a0020.
89. Weissmann, G.S., Mount, J.F., and Fogg, G.E., 2002a, Glacially driven cycles in accumulation space and sequence stratigraphy of a stream dominated alluvial fan, San Joaquin Valley, California, U.S.A.: Journal of Sedimentary Research, v. 72, no. 2, p. 240–251.
90. Weissmann, G.S., Zhang, Y., LaBolle, E.M., and Fogg, G.E., 2002b, Dispersion of groundwater age in an alluvial aquifer system: Water Resources Research, v. 38, p. 1198–1211, doi: 10.1029/2001WR000907.
91. White A.F., Blum A.E., Schulz M.S., Bullen T.D., Harden J.W., Peterson M.L., 1996. Chemical weathering rates of a soil chronosequence on granitic alluvium: I. Quantification of mineralogical and surface area changes and calculation of primary silicate reaction rates. Geochimica et Cosmochimica Acta, Vol. 60, No. 14, pp. 2533-2550
92. White, K.E., Brennan, E.B., Cavigelli, M.A., Smith, R.F., 2020. Winter cover crops increase readily decomposable soil carbon , but compost drives total soil carbon during eight years of intensive , organic vegetable production in California. PLoS One 15. https://doi.org/https://doi. org/10.1371/journal.pone.0228677
93. Wu Y, Ajo-Franklin JB, Spycher N et al (2011) Geophysical monitoring and reactive transport modeling of ureolyti- cally-driven calcium carbonate precipitation. Geochem Trans 12:7. doi:10.1186/1467-4866-12-7
94. Xiang, S.-R., Doyle, A., Holden, P.A., Schimel, J.P., 2008. Drying and rewetting effects on C and N mineralization and microbial activity in surface and subsurface California grassland soils. Soil Biol. Biochem. 40, 2281–2289. http://dx.doi.org/10.1016/j. soilbio.2008.05.004.
95. Xu, T., Sonnenthal, E. L., Spycher, N., and Zheng, L. (2017), TOUGH- REACT—A simulation program for non-isothermal multiphase reactive geochemical transport in variably saturated geologic media: Applications to geothermal injectivity and CO2 geological sequestration, Comput. Geosci., 32(2), 145–165.
96. Yabusaki, S.B., Wilkins, M.J., Fang, Y., Williams, K.H., Arora, B., Bargar, J., Beller, H.R., Bouskill, N.J., Brodie, E.L., Christensen, J.N., Conrad, M.E., Danczak, R.E., King, E., Soltanian, M.R., Spycher, N.F, Steefel, C.I., Tokunaga, T.K., Versteeg, R., Waichler, S.R., Wainwright, H.M. *Environmental Science & Technology* **2017** *51* (6), 3307-3317 DOI: 10.1021/acs.est.6b04873
    Yeomans, J. C., Bremner, J. M., & McCarty, G. W. (1992). Denitrification capacity and denitrification potential of subsurface soils. *Communications in Soil Science and Plant Analysis*, *23*(9–10), 919–927. https://doi.org/10.1080/00103629209368639

Table 1: Soil properties averaged by depth (per meter) with standard errors in parentheses (n=5/meter).

Depth	**Sand**	**Silt**	**Clay**	**Total N**	**Total C**	**NO_3^--N**	**pH**
(cm-bgs)	**(%)**	**(%)**	**(%)**	**(%)**	**(%)**	**(ug/g)**	

0-25	46.24 (7.68)	46.13 (7.49)	7.64 (0.72)	0.048 (0.01)	0.73 (0.11)	10.19 (4.18)	6.71 (0.15)
100-200	42.41 (6.49)	48.64 (5.53)	8.95 (2.64)	0.050 (0.03)	0.21 (0.04)	13.81 (4.63)	6.99 (0.10)
200-300	48.39 (9.57)	43.19 (8.16)	8.43 (2.57)	0.050 (0.03)	0.068 (0.02)	5.09 (1.38)	6.99 (0.09)
300-400	56.09 (9.93)	37.64 (8.36)	6.27 (1.71)	0.010 (0.01)	0.048 (0.02)	3.26 (1.07)	6.99 (0.10)
400-500	78.96 (8.13)	18.12 (7.42)	2.92 (0.78)	0.004 (0.001)	0.056 (.03)	1.11 (0.34)	6.92 0.07)
500-600	55.60 (7.39)	33.34 (5.54)	11.06 (2.14)	0.006 (0.001)	0.065 (0.02)	1.37 (0.31)	7.07 (0.07)
600-700	60.56 (8.05)	35.38 (7.47)	4.06 (1.21)	0.060 (0.05)	0.035 (0.02)	0.57 (0.13)	7.18 (0.07)
700-800	75.45 (4.93)	16.59 (3.63)	7.96 (1.44)	0.120 (0.07)	0.027 (0.01)	0.83 (0.17)	7.26 (0.09)
800-900	84.11 (4.27)	10.56 (3.63)	5.33 (1.35)	0.020 (0.01)	0.099 (0.02)	1.71 (0.37)	7.17 (0.11)

Table 2: Aqueous concentrations of primary species applied as fixed concentrations at the top of the model boundary and in the flood water. Concentrations are in mol L^{-1}, unless otherwise specified.

	Initial Water	**Flood Water**
pH$^{(a)}$	7.5	8^{b}
$O_{2\,(aq)}$	2.09×10^{-4}	2.09×10^{-4} ^{c}
$SiO_{2\,(aq)}$	6.83×10^{-4}	6.83×10^{-6}
Na^+	1.83×10^{-3}	1.83×10^{-5}
K^+	7.42×10^{-5}	7.42×10^{-7}
Ca^{2+}	9.74×10^{-4} ^{d}	9.74×10^{-6}
Mg^{2+}	3.50×10^{-4}	3.50×10^{-6}
HCO_3^-	4.06×10^{-3} ^{d}	1.65×10^{-5} ^{e}
SO_4^{2-}	1.25×10^{-4}	1.25×10^{-6}
Cl^-	6.77×10^{-4}	6.77×10^{-4}
HS^-	1.00×10^{-20}	1.00×10^{-20}
NO_3^-	7.14×10^{-4}	7.14×10^{-6}
NO_2^-	9.35×10^{-7}	9.35×10^{-9}

N_2	1.00×10^{-20}	1.00×10^{-20}
$NH_{3\,(aq)}$	1.00×10^{-8}	1.00×10^{-9}
Al^{3+}	6.70×10^{-10} (f)	1.00×10^{-20}
Fe^{3+}	1.16×10^{-19} (g)	1.00×10^{-20}
Fe^{2+}	8.30×10^{-20}	8.30×10^{-20}
Ba^{2+}	4.15×10^{-7}	1.00×10^{-20}
Sr^{2+}	5.17×10^{-6}	1.00×10^{-20}
Acetate	1.19×10^{-5} (h)	1.19×10^{-7} (h)

(a) pH units
(b) adjusted for charge balance
(c) Fixed by P_{O2} (g) of $10^{-0.7}$ bar
(d) Fixed by equilibrium with calcite
(e) Fixed by P_{CO2} (g) of $10^{-3.4}$ bar
(f) Fixed by equilibrium with k-feldspar
(g) Fixed by equilibrium with ferrihydrite

(h) Fixed by equilibrium with cellulose

Table 3: Hydraulic parameters used in this study. $K_{s,z}$ is the saturated hydraulic conductivity in the vertical direction, θ_r and θ_s are the residual and saturated volumetric water content, α is related to the inverse of the air entry pressure value, and n is soil water retention curve shape parameter.

Soil Type	**Permeability, k (m^2)**	**$K_{s,z}$ (cm/hr)**	**van Genuchten-Mualem Parameters**			
			n (-)	**α** (cm^{-1})	**θ_r** (-)	**θ_s** (-)
Top Layer - Modified Loam	4.8×10^{-14}	0.17	1.31	0.019	0.095	0.43
Limiting Layer	1.4×10^{-14}	0.05	1.09	0.008	0.068	0.48
Silt Loam	1.3×10^{-13}	0.45	1.41	0.02	0.067	0.46
Sandy Loam	1.3×10^{-12}	4.4	1.89	0.075	0.065	0.41

Table 4: Microbially mediated redox reactions, their thermodynamic and kinetic parameters considered in the reactive transport model.

Reaction	**Log K (25 °C)(a)**	**K_{max}**	**K_s**	**$K_{inibitor}$**
		(mol L^{-1} s^{-1})	**(mol L^{-1})**	**(mol L^{-1})**
$CH_3COO^- + 2O_2 \rightarrow 2HCO_3^- + H^+$	146.76	1.0 x 10^{-11} (b)	O_2: 2.41 x 10^{-5} (d)	
$CH_3COO^- + 4NO_3^- \rightarrow 2HCO_3^- + 4NO_2^- + H^+$	89.04	2.78 x 10^{-10}(c)	NO_3^-:1.13 x 10^{-4} (d)	O_2: 3.22 x 10^{-7} (e)
$CH_3COO^- + 2.667NO_2^- + 1.667H^+ \rightarrow 2HCO_3^- + 1.33N_2 + 1.33H_2O$	200.52	3.47 x 10^{-8} (c)	NO_2^-: 1.13 x 10^{-4} (d)	O_2: 3.22 x 10^{-7} (e)
$NH_3(aq) + 2O_2 \rightarrow NO_3^- + H_2O + H^+$	62.23	5.27 x 10^{-2} (b)	NH_3: 1.48 x 10^{-5} (f) O_2: 2.41 x 10^{-5} (d)	
$CH_3COO^- + 8Fe^{+3} + 4H_2O \rightarrow 8Fe^{+2} + 2HCO_3^- + 9H^+$	79.00	1.0 x 10^{-14} (b)		O_2: 3.22 x 10^{-7} (e) NO_3^-: 1.0 x 10^{-7} (g)
$Fe^{+2} + 0.2NO_3^- + 1.2H^+ \rightarrow Fe^{+3} + 0.1N_2 + 0.6H_2O$	-7.32	7.0 x 10^{-10} (h)	Fe^{+2}: 1.0 x 10^{-5} (i) NO_3^-:1.13 x 10^{-4} (d)	O2: 3.22 x 10^{-7} (e) NO3-: 1.0 x 10^{-7} (g)
$CH_3COO^- + SO_4^{-2} \rightarrow 2HCO_3^- + HS^-$	8.40	3.0 x 10^{-12} (b)	SO_4^{-2}: 1.0 x 10^{-3} (i)	O_2: 3.22 x 10^{-7} (e) NO_3^-: 1.0 x 10^{-7} (g) Fe^{+3}: 1.0 x 10^{-12} (b)
$HS^- + 1.6NO_3^- + 0.6H^+ \rightarrow SO_4^{-2} + 0.8N_2 + 0.8H_2O$	11.52	7.0 x 10^{-10} (j)	HS^-: 1.0 x 10^{-5} (k) NO_3^-: 1.13 x 10^{-4} (d)	O_2: 3.22 x 10^{-7} (e)

(a)Calculated from log*K* values for half redox reactions reported by (Morel and Hering 1993); (b)Adapted from Arora et al. 2016; (c)Calibrated using denitrification capacity assays; (d)Taken from Maggi et al. 2008; (e)Taken from Bonin et al. 1989; (f)Taken from Wu et al. 2011; (g) Taken from Doussan et al. 1997; (h)Adapted from Palmer et al. 2010; (i)Taken from Mayer et al. 2002; (j) Kept to yield maximum reaction rate similar to that of NO_3^- reduction by Fe^{+2}; (k)Taken from Handley et al. 2013

Table 5: Results of cluster analysis on soil core and acetylene inhibition incubation data. Medians are shown with minimum and maximum values in parentheses.

	Soil Classification	**Total N_2O**	**Total CO_2**	**TOC**	**NO_3^-**	**Fe**	**S**
		ug g^{-1}	**ug g^{-1}**	**%**	**ug g^{-1}**	**ug g^{-1}**	**ug g^{-1}**
1	Sandy Loam top meter	1.62 (1.46-1.72)	175.30 (74.70-587.35)	0.18 (0.01 - 0.29)	1.20 (1.19 - 2.64)	14.77 (10.94 - 20.66)	0.44 (0.33 - 0.47)
2	Silt Loam below one meter	0.53 (0.40 - 0.80)	35.70 (15.10 -61.97)	0.07 (0.03 - 0.16)	1.01 (0.80 - 1.84)	12.02 (8.64 - 14.96)	0.69 (0.41 - 1.20)
3	Sand and Sandy Loam below one meter	0.05 (0.01 - 0.015)	10.70 (0.0 - 59.40)	0.06 (0.03 - 0.10)	0.25 (0.0 - 0.70)	10.43 (7.27-16.34)	0.44 (0.24 - 1.01)

List of Figures

Figure 1: Conceptual diagram of modeling scenarios including the five stratigraphy scenarios overlain by each AgMAR management scenario (S1 to S3).

Figure 2: Map of study area in Modesto, CA with a picture of the actual field site during an AgMAR flooding event.

Figure 3: Electrical resistivity tomography image of a 2D transect at our field site. More conductive layers correspond to finer materials and are in blue and more resistive layers correspond to coarser materials and are in red. Areas where specific textural classifications are given correspond to where texture analysis was conducted on physically cored samples.

Figure 4: Sandy loam with silt loam channel (SaSi case) predicted liquid saturation, NO_3^-:Cl^- ratios, and NO_3^- (mol L^{-1}) profiles at pre-flood steady state (A, B, and C, respectively) and 60 days from start of flooding for S1 (D, E, F). Depth (Z) is in meters below the ground surface with the water table at 15 m-bgs.

Figure 5: Silt loam with sandy loam channel (SiSa case) predicted liquid saturation, NO_3^-:Cl^- ratios, and NO_3^- (mol L^{-1}) profiles at pre-flood steady state(A, B, and C, respectively) and 60 days from start of flooding for S1 (D, E, F). Depth (Z) is in meters below the ground surface with the water table at 15 m-bgs.

Figure 6: Predicted NO_3^-:Cl (A and B), pH (C and D), and total $Iron_{aq}$ (E and F) (mol L^{-1}) profiles for the homogeneous sandy loam vs. homogeneous silt loam stratigraphies at pre-flood steady state. Depth (Z) is in meters below the ground surface with the water table at 15 m-bgs.

Figure 7: Percent of NO_3^- denitrified for each stratigraphy and flooding scenario.

Figure 8: Simplified ERT predicted acetate (mol L^{-1}) , O_2 (mol L^{-1}), NO_3^- (mol L^{-1}) profiles, NO_3^- :Cl^- ratios at pre-flood steady state (A, B, C, and D respectively) and 60 days from start of flooding for S1 (E, F, G and H). Depth (Z) is in meters below the ground surface with the water table at 15 m-bgs.

Figure 9: A) Saturation, B) NO_3^- (mol L^{-1}), C) ratio of NO_3^- to Cl^- and D) Acetate concentrations (mol L^{-1}), and over time by depth within each AgMAR scenario(S1, S2, S3) adjacent to the preferential flow channel for the Simplified ERT profile.

Figure 10: A) $O_{2\,(aq)}$ concentrations (mol L^{-1}), B) NO_3^- (mol L^{-1}), and C) ratio of NO_3^- to Cl^- over time by depth within AgMAR scenarios (S1 and S2) for different antecedent moisture conditions adjacent to the preferential flow channel.

Hydraulic Loading

Scenario 1 (S1)
Amount of water Applied: 68cm
Frequency: Once
Duration: One Time
Total Water Applied: 68cm

Scenario 2 (S2)
Amount of water Applied: 17cm
Frequency: 1x per week
Duration: 4 weeks
Total Water Applied: 68cm

Scenario 3 (S3)
Amount of water Applied: 17cm
Frequency: 2x per week
Duration: 2 weeks
Total Water Applied: 68cm

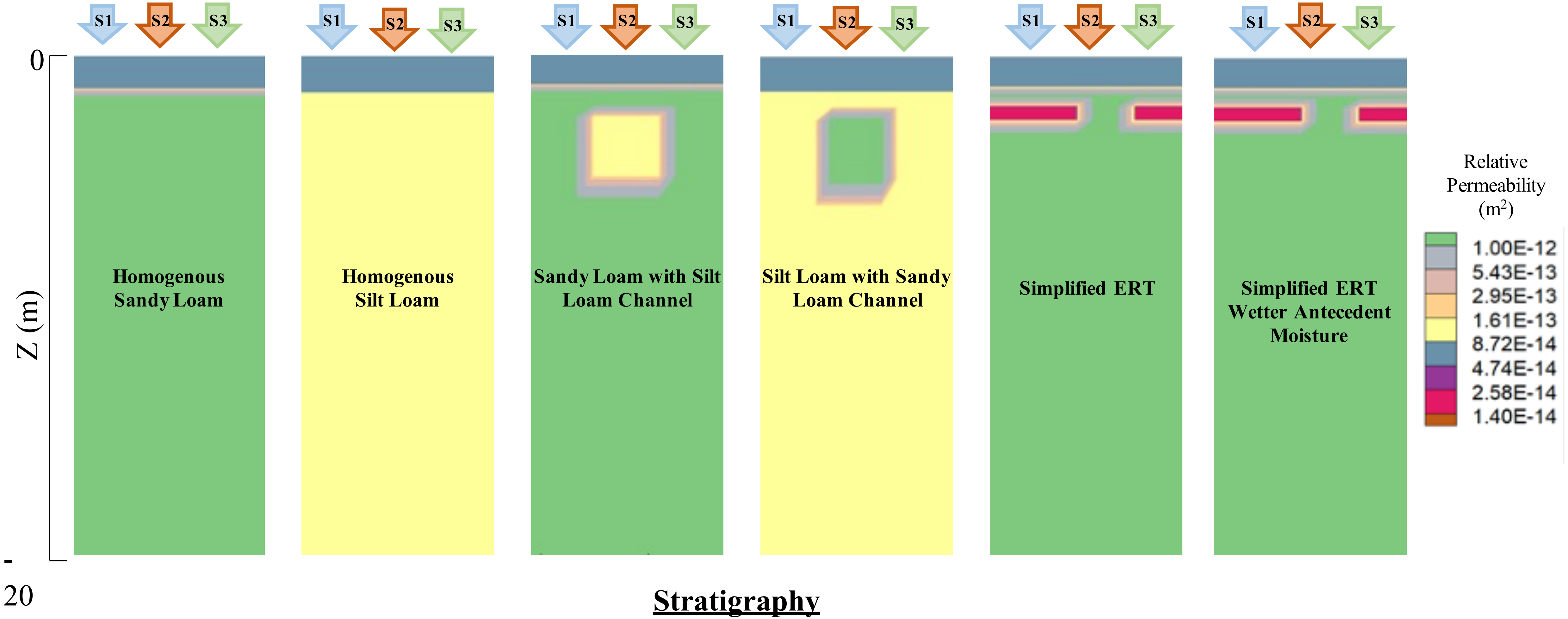

Stratigraphy

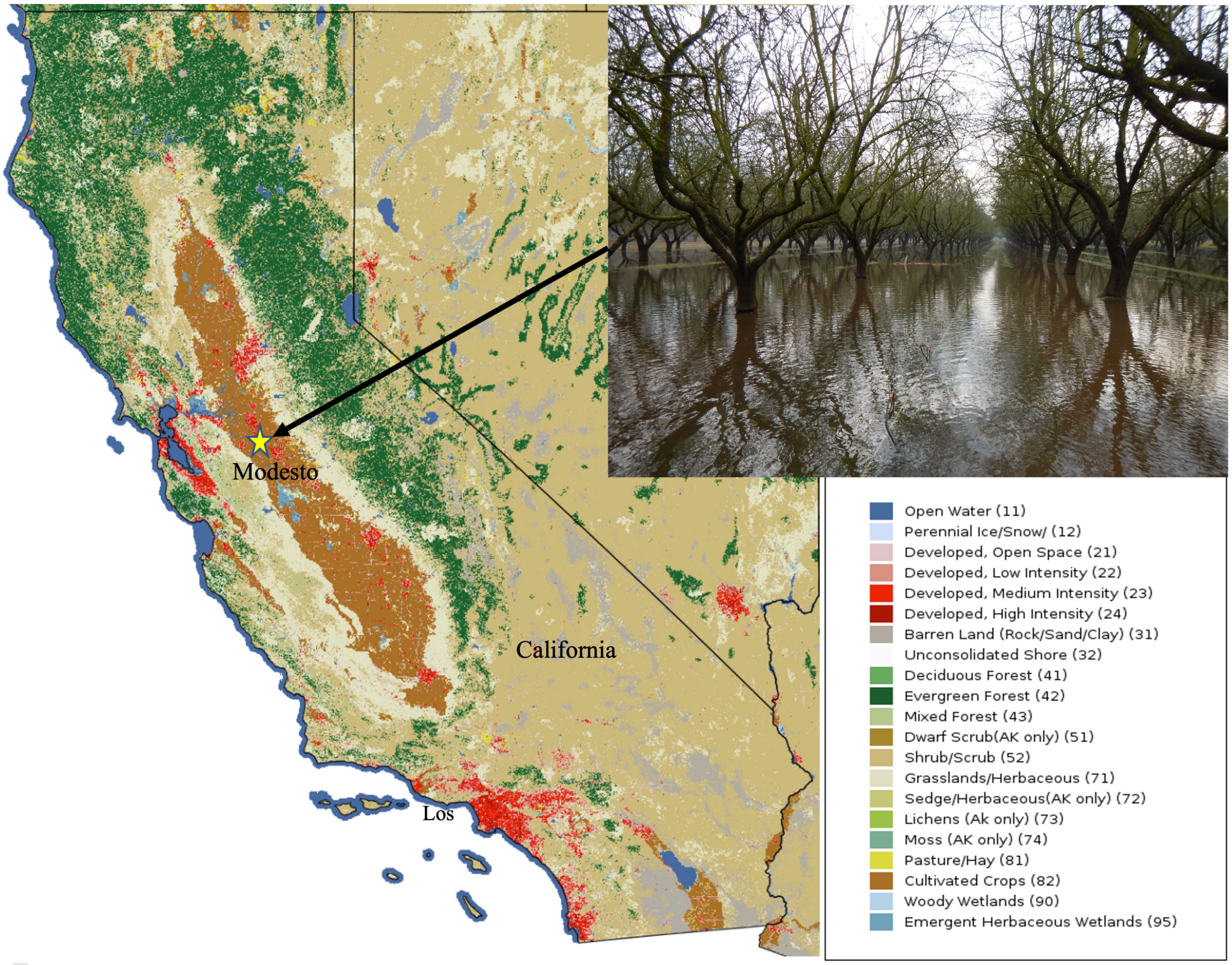
Modesto
California
Los
Open Water (11)
Perennial Ice/Snow/ (12)
Developed, Open Space (21)
Developed, Low Intensity (22)
Developed, Medium Intensity (23)
Developed, High Intensity (24)
Barren Land (Rock/Sand/Clay) (31)
Unconsolidated Shore (32)
Deciduous Forest (41)
Evergreen Forest (42)
Mixed Forest (43)
Dwarf Scrub(AK only) (51)
Shrub/Scrub (52)
Grasslands/Herbaceous (71)
Sedge/Herbaceous(AK only) (72)
Lichens (Ak only) (73)
Moss (AK only) (74)
Pasture/Hay (81)
Cultivated Crops (82)
Woody Wetlands (90)
Emergent Herbaceous Wetlands (95)

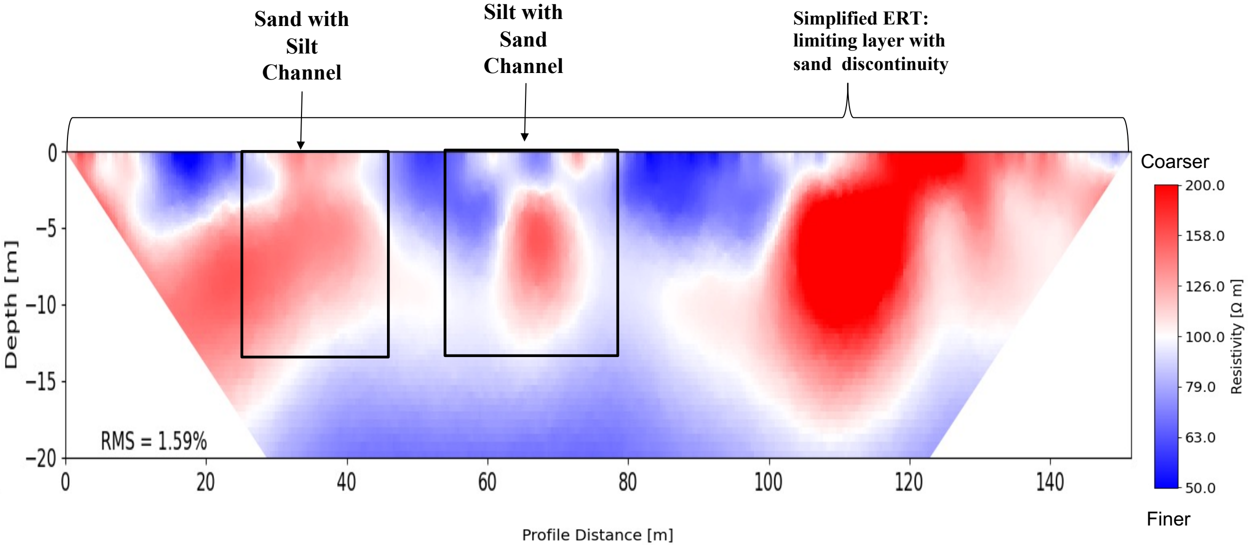
Sand with Silt Channel
Silt with Sand Channel
Simplified ERT: limiting layer with sand discontinuity
0
−5
−10
−15
−20
Depth [m]
RMS = 1.59%
0
20
40
60
80
100
120
140
Profile Distance [m]
Coarser
200.0
158.0
126.0
100.0
79.0
63.0
50.0
Resistivity [Ω m]
Finer

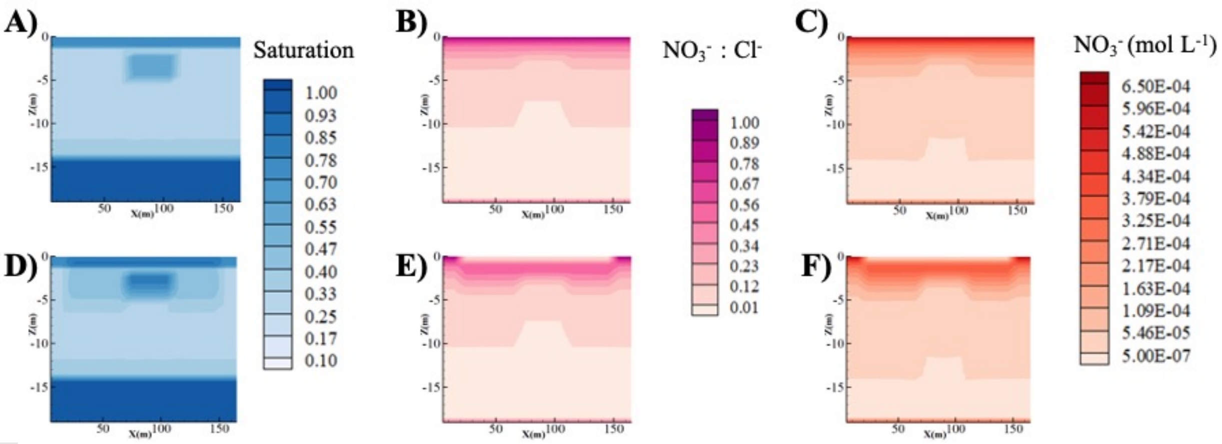
A)
B)
C)
D)
E)
F)
Saturation
1.00
0.93
0.85
0.78
0.70
0.63
0.55
0.47
0.40
0.33
0.25
0.17
0.10
NO3- : Cl-
1.00
0.89
0.78
0.67
0.56
0.45
0.34
0.23
0.12
0.01
NO3- (mol L-1)
6.50E-04
5.96E-04
5.42E-04
4.88E-04
4.34E-04
3.79E-04
3.25E-04
2.71E-04
2.17E-04
1.63E-04
1.09E-04
5.46E-05
5.00E-07
Z(m)
0
-5
-10
-15
X(m)
50
100
150

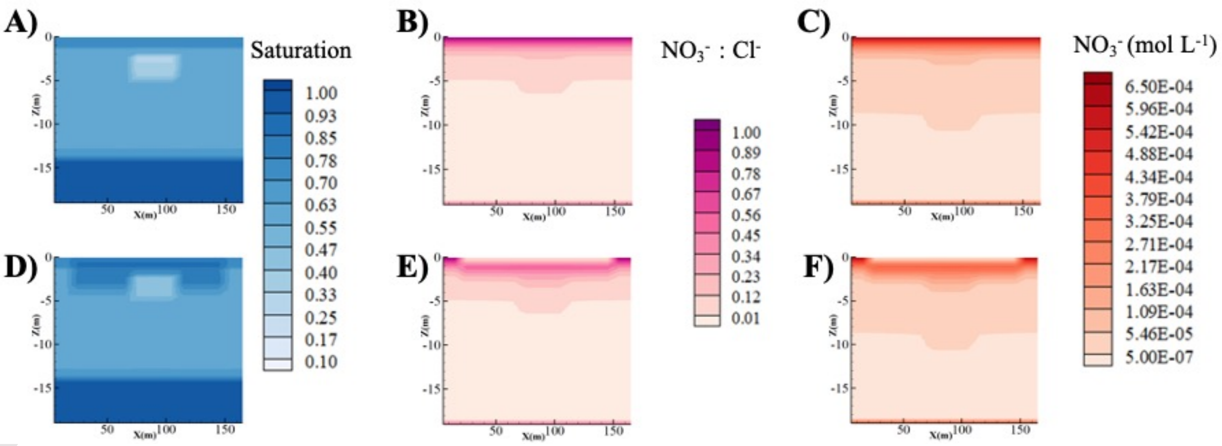
A)
B)
C)
D)
E)
F)
Z(m)
X(m)
0
-5
-10
-15
50
100
150
Saturation
1.00
0.93
0.85
0.78
0.70
0.63
0.55
0.47
0.40
0.33
0.25
0.17
0.10
NO_3^- : Cl^-
1.00
0.89
0.78
0.67
0.56
0.45
0.34
0.23
0.12
0.01
NO_3^- (mol L^{-1})
6.50E-04
5.96E-04
5.42E-04
4.88E-04
4.34E-04
3.79E-04
3.25E-04
2.71E-04
2.17E-04
1.63E-04
1.09E-04
5.46E-05
5.00E-07

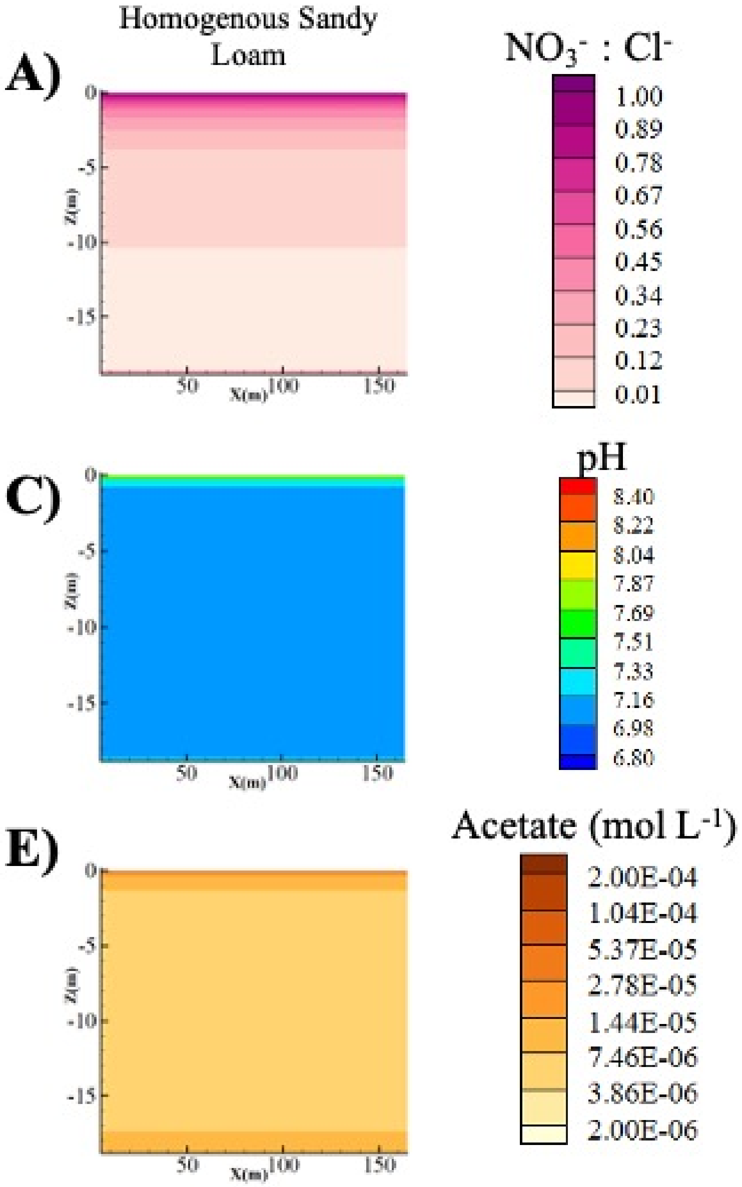

Homogenous Sandy Loam
Homogenous Silt Loam
A)
B)
C)
D)
E)
F)
NO$_3^-$: Cl$^-$
1.00
0.89
0.78
0.67
0.56
0.45
0.34
0.23
0.12
0.01
pH
8.40
8.22
8.04
7.87
7.69
7.51
7.33
7.16
6.98
6.80
Acetate (mol L^{-1})
2.00E-04
1.04E-04
5.37E-05
2.78E-05
1.44E-05
7.46E-06
3.86E-06
2.00E-06
Z(m)
0
-5
-10
-15
X(m)
50
100
150

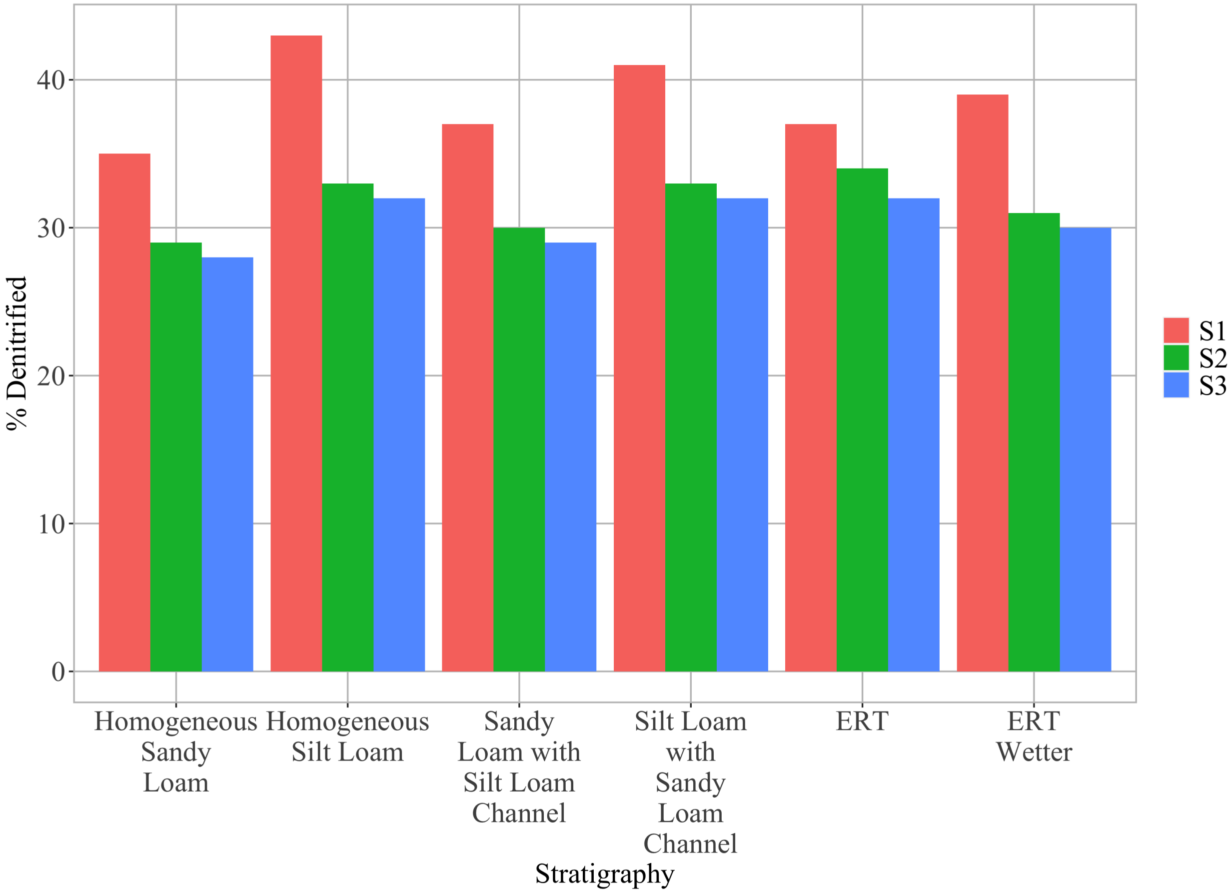
40
30
20
10
0
% Denitrified
Homogeneous Sandy Loam
Homogeneous Silt Loam
Sandy Loam with Silt Loam Channel
Silt Loam with Sandy Loam Channel
ERT
ERT Wetter
Stratigraphy
S1
S2
S3

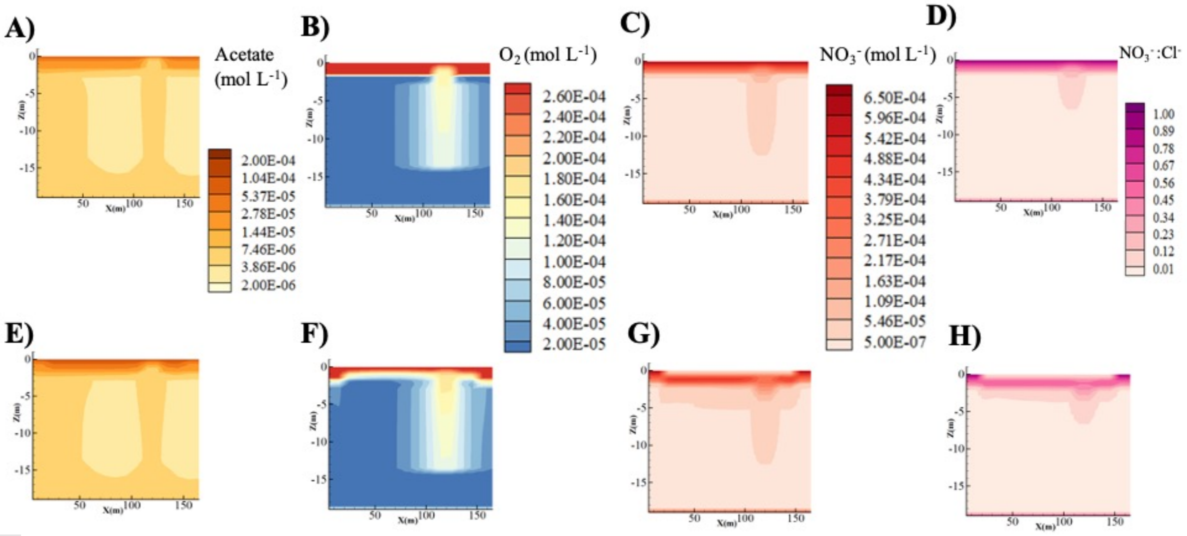
A)
Acetate (mol L-1)
2.00E-04
1.04E-04
5.37E-05
2.78E-05
1.44E-05
7.46E-06
3.86E-06
2.00E-06
B)
O2 (mol L-1)
2.60E-04
2.40E-04
2.20E-04
2.00E-04
1.80E-04
1.60E-04
1.40E-04
1.20E-04
1.00E-04
8.00E-05
6.00E-05
4.00E-05
2.00E-05
C)
NO3- (mol L-1)
6.50E-04
5.96E-04
5.42E-04
4.88E-04
4.34E-04
3.79E-04
3.25E-04
2.71E-04
2.17E-04
1.63E-04
1.09E-04
5.46E-05
5.00E-07
D)
NO3-:Cl-
1.00
0.89
0.78
0.67
0.56
0.45
0.34
0.23
0.12
0.01
E)
F)
G)
H)
Z(m)
0
-5
-10
-15
X(m)
50
100
150

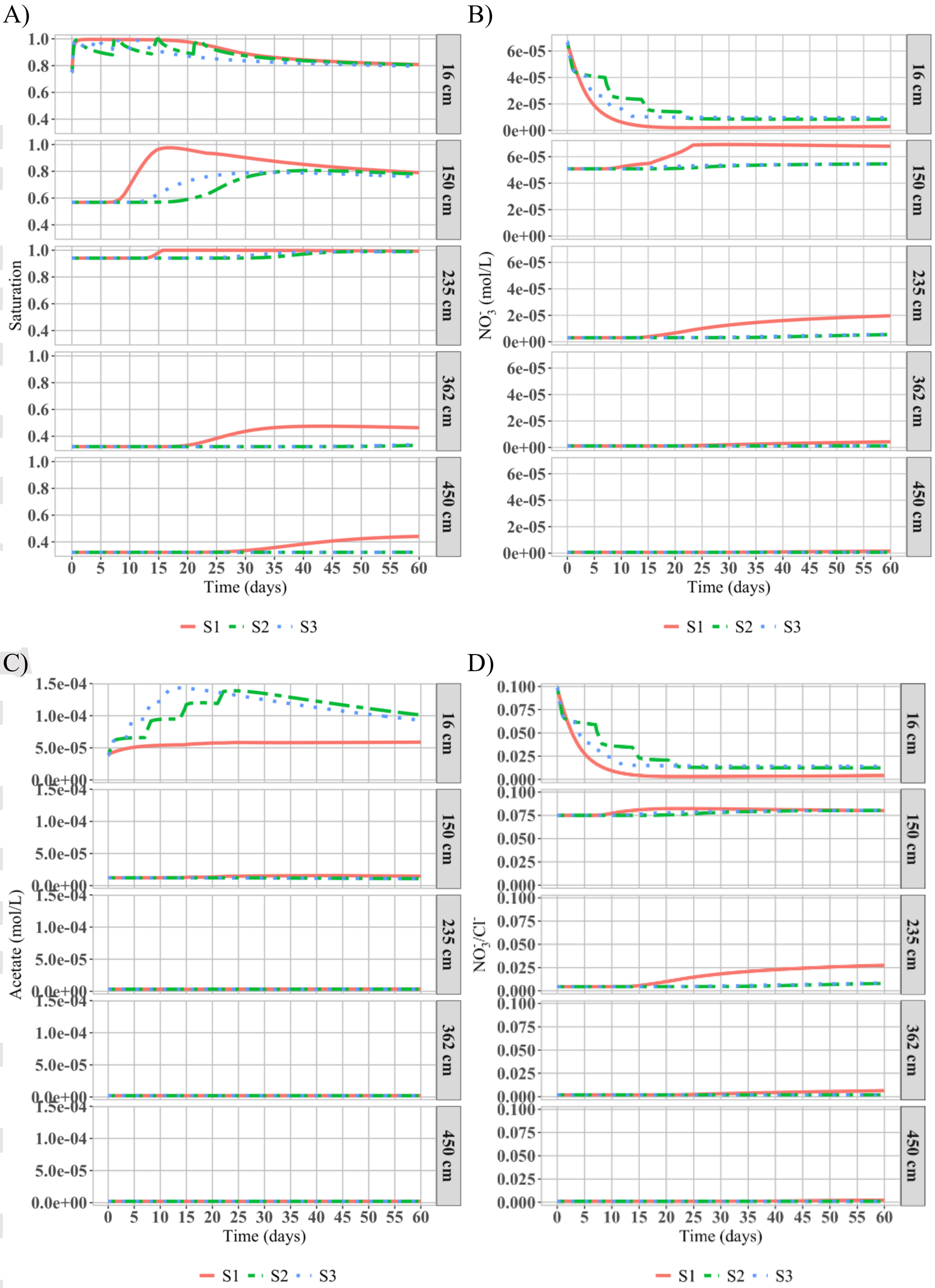
A)
B)
C)
D)
Saturation
NO$_3^-$ (mol/L)
Acetate (mol/L)
NO$_3^-$/Cl$^-$
16 cm
150 cm
235 cm
362 cm
450 cm
Time (days)
0 5 10 15 20 25 30 35 40 45 50 55 60
0.4 0.6 0.8 1.0
0e+00 2e-05 4e-05 6e-05
0.0e+00 5.0e-05 1.0e-04 1.5e-04
0.000 0.025 0.050 0.075 0.100
S1
S2
S3

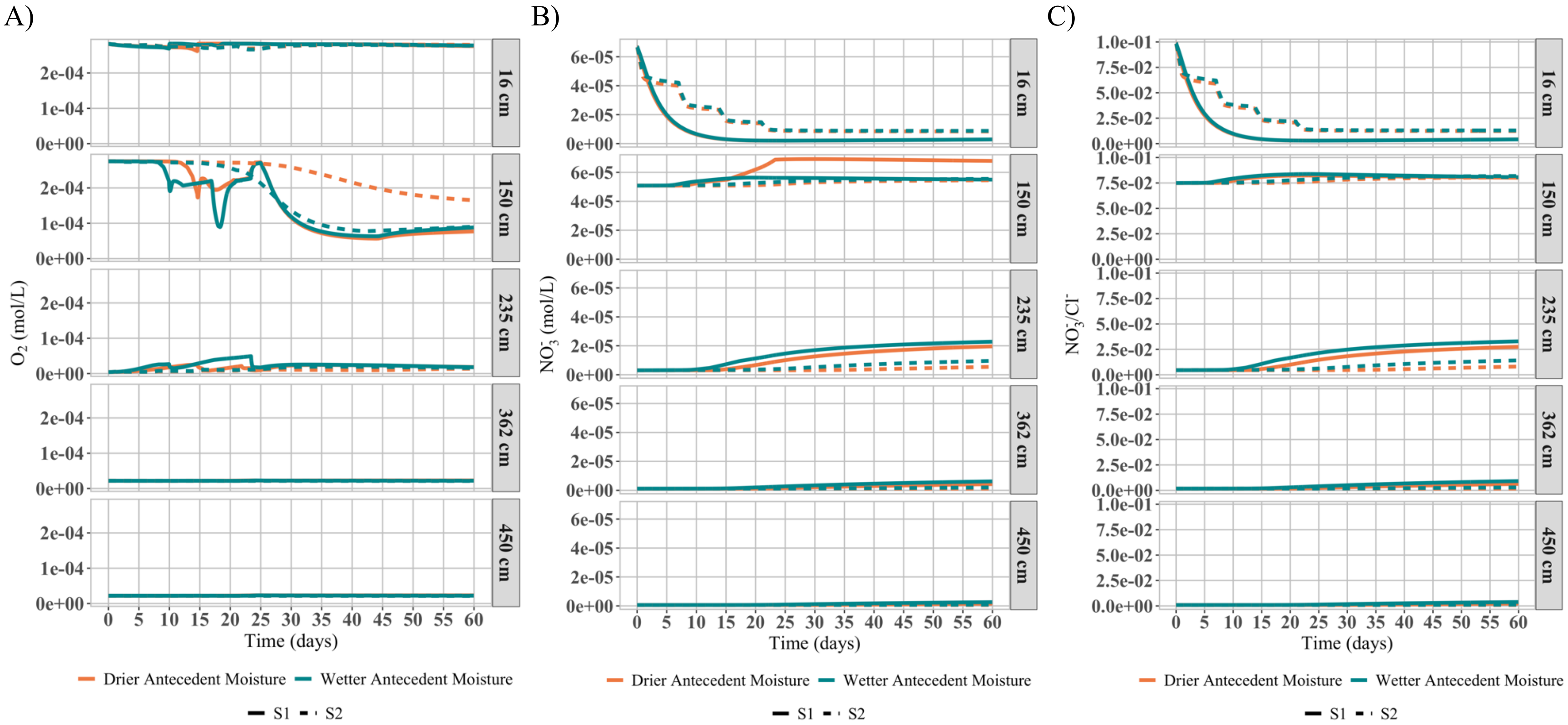
A)
B)
C)
O₂ (mol/L)
NO₃⁻ (mol/L)
NO₃⁻/Cl⁻
16 cm
150 cm
235 cm
362 cm
450 cm
0e+00
1e-04
2e-04
0e+00
2e-05
4e-05
6e-05
0.0e+00
2.5e-02
5.0e-02
7.5e-02
1.0e-01
0 5 10 15 20 25 30 35 40 45 50 55 60
Time (days)
Drier Antecedent Moisture
Wetter Antecedent Moisture
S1
S2